SEASONAL VARIABILITY IN PARTICLE FLUX ATTENUATION IN THE GLOBAL OCEAN GENERATES SPATIAL VARIABILITY IN ANNUAL TRANSFER EFFICIENCY

F. DE MELO VIRÍSSIMO[1,2,*], A. P. MARTIN[1], S. A. HENSON[1], J. D. WILSON[3,4]

[1] *National Oceanography Centre, Southampton, SO14 3ZH, United Kingdom*
[2] *Grantham Research Institute on Climate Change and the Environment, London School of Economics and Political Science, London, WC2A 2AE, United Kingdom*
[3] *School of Earth Sciences, University of Bristol, Bristol, BS8 1QU, United Kingdom*
[4] *Department of Earth, Ocean and Ecological Sciences, University of Liverpool, Liverpool, L69 3GP, United Kingdom*

NOTE: THIS IS A NON-PEER REVIEWED PREPRINT SUBMITTED TO EARTHARXIV

Abstract. The biological carbon pump consists of a collection of coupled physical and biogeochemical processes, which together transport large quantities of carbon from the ocean surface to the interior. The efficiency of this transport can vary geographically, and understanding this variation and its causes is paramount, since it impacts how much carbon dioxide is sequestered by the ocean. The variability in this transfer efficiency is still poorly constrained, and there is no current consensus for its cause, with previous global compilations being inconclusive on whether it is higher at higher latitudes than in the tropics or vice versa. Here, we use a global ocean-biogeochemical model to show that seasonal variability in a spatially uniform flux attenuation can lead to spatial variability emerging in annual mean transfer efficiency that matches observations of being higher at high latitudes than in low latitudes. We also show that this approach can explain the differences between different transfer efficiency compilations, as being due to the time and duration of sampling, as well as the methodology used to derive the results. Our results suggest caution in the mechanistic interpretation of annual-mean patterns in transfer efficiency and demonstrates the need for consistent sampling in time to generate accurate estimates of the biological carbon pump that can be used to constrain our understanding. It also suggests that incorporating a mechanistic model for sinking and attenuation that reproduces observed seasonal cycles is necessary to understand how the biological carbon pump will impact the carbon cycle in response to climate change.

Significance statement. Each year, marine phytoplankton convert carbon dioxide (CO_2) into tonnes of organic carbon with a fraction of it reaching the deep ocean, where it can remain for hundreds of years. The efficiency of this surface-to-depth carbon transfer is therefore a key determinant of the atmosphere-ocean CO_2 balance. However, its variability and underlying causes are poorly understood, to the extent that different studies report contradicting results. We show that the existence of seasonal variability in the attenuation of sinking carbon particles may explain the observed spatial variability in annual transfer efficiency and reconcile with the literature. Our findings suggest caution in interpreting results from sparse but time-varying datasets, highlighting that seasonal variability should be considered when studying the oceanic carbon cycle.

Keywords: biological carbon pump, carbon transfer efficiency, seasonality in flux attenuation, mesopelagic ocean, sinking speed, remineralisation

*Corresponding Author. e-mail: f.de-melo-virissimo@lse.ac.uk.

Author contributions: F.d.M.V. designed the study and performed all simulations and analyses. F.d.M.V. wrote the manuscript with input from A.P.M., S.A.H. and J.D.W.

The authors declare no conflict of interest.

Introduction

The biological carbon pump (BCP) is an ubiquitous component of the ocean's carbon cycle [1]. In this process, marine phytoplankton assimilate dissolved carbon dioxide (CO_2) in the sunlit, ocean surface (top 100m) to produce around 50 Pg of organic carbon per year [2]. While most of this organic carbon production is quickly respired back into inorganic carbon, about 10-20% of it is exported [3] as particulate organic carbon (POC) from surface waters into the mesopelagic ocean (100-1,000m). Eventually, part of this POC reaches the deep, bathypelagic ocean (below 1,000m), where it may remain for hundreds of years [4] before reaching the surface ocean again as dissolved inorganic carbon (DIC). Through this process, the BCP is estimated to have lowered the baseline atmospheric concentration of CO_2 by more than 50% of with respect to the effects of physical and chemical equilibrium alone [5].

In this biogeochemical journey, there are essentially two contrasting processes which determine the fate of the exported POC: sinking and remineralisation. As POC sinks downward it is remineralised by being broken down and respired by heterotrophic organisms on the way. It is the balance between these processes that determines the efficiency of the BCP in transferring detritus to the deep ocean. For example, given a remineralisation rate, the faster the POC sinks, the more of it will survive the journey, with a higher fraction reaching the deep ocean. The 'transfer efficiency' (hereafter TE) is defined as the ratio between the POC flux at 1,000m divided by the export flux (typically at 100m).

Several mechanisms are thought to control sinking speed and remineralisation rates: sinking speed can depend on the composition and shape of the particle [6, 7], particle fragmentation by zooplankton [8, 9], aggregation and other factors such as ballast [10, 11]. Remineralisation rate may be dependent on the nature of the particle [12], microbial colonisation and degradation [13, 14], temperature- and oxygen-dependence of metabolic rates [15], and many other factors. Furthermore, recent lab-based evidence suggests that these processes might be coupled, such that faster sinking could enhance bacterial degradation for instance [16].

In practice, TE is usually estimated from a model or observations through particle flux curves, the most popular being the so-called Martin curve [17, 18]. This formulation states that TE equals the ratio of the export depth and the transfer depth to the power of an exponent, say b, where the exponent b can be estimated from flux data (Supporting Information). From a mechanistic point of view, b can be expressed as the ratio between sinking and remineralisation rates (Equation [7] in Supporting Information). For this reason, b is usually referred to as the flux attenuation exponent. Since the proposal of such parameterisations for the BCP, they have been widely used in both data and model-based studies, often with the flux attenuation exponent assuming Martin's original value of $b = 0.858$ [17].

Evidence from observation and model-based studies suggest the flux attenuation exponent, and therefore TE, is significantly variable. For instance, a series of independent field-based investigations [19, 20, 21, 6, 22] estimated values of b between 0.5 and 2.0 across the ocean, later used as the basis to assess the influence of remineralisation depth changes on atmospheric pCO_2 [23, 24]. Several global compilations for TE have been proposed since, with two of them standing out: a compilation of thorium-derived export fluxes and sediment-trap fluxes at 2,000m [25], which found TE to be lower at low latitudes and high at high latitudes, and a compilation obtained from a limited set of eight data points collected with neutrally-buoyant mesopelagic sediment-traps from the North Atlantic and Pacific, which showed the opposite pattern [26]. Later studies using data-constrained modelling [27, 28, 29] obtained TE distributions that agreed with the latter, but were not able to explain why they differ from the former. More recently, there have been additional evidence for seasonal variability in TE [30, 31], with numerical experiments showing that addition of seasonal variability of 60% (about the mean) in the flux attenuation parameter more than doubles the sequestration of carbon predicted by an ocean-biogeochemical model [32].

The importance of variability in flux attenuation, and hence TE, goes beyond its measure of POC fluxes and carbon sequestration. For instance, the spatial patterns can be used to infer net dominant processes such as temperature-dependent remineralisation or ballasting, which can then be used to make predictions of how carbon sequestration by the BCP may change as a response to changes in those processes.

Despite the evidence for, and the importance of temporal and spatial variability in the flux attenuation and its potential influence on carbon sequestration, both sinking and remineralisation - as well as the flux attenuation parameter - are often assumed to be constant both in space and time. This is also the case in higher complexity models such as the CMIP6 generation [33, 34], which have mechanistic representations of remineralisation but often model detritus as sinking at a constant speed.

Here, we demonstrate the importance of resolving seasonality in the BCP with two key results: first, we use a global ocean-biogeochemical model to link seasonal to spatial variability by showing that a seasonally-varying flux attenuation is, by itself, sufficient to generate spatial variability in TE, with a resulting global distribution of annual TE that agrees with those presented in the literature [26, 27, 28, 29]. Second, we show that considering seasonality allows the reconciliation of the apparently conflicting results for global annual TE spatial patterns discussed above [25, 26].

In what follows, we apply a uniform but seasonally-varying flux attenuation of particulate organic carbon within a coupled global ocean-biogeochemical model. To allow a comparison between the constant and seasonal flux attenuation scenarios, we assume that the detritus is not transported by circulation and can only sink vertically, as assumed in the data-constrained modelling study [27]. For full details of the model and assumptions used, please see the Materials and methods section and the Supporting Information.

Spatial variability in transfer efficiency

In the absence of seasonal variability in the model's flux attenuation b^{model} and sinking speed (see Materials and Methods; see Supporting Information), the annual mean TE is spatially invariant throughout the ocean†. This is shown in Fig. S2 (Supporting Information) for the model's original value of $b^{\mathrm{model}} = 1.388$, which means that TE ≈ 0.04738 as predicted by the Martin curve (see Supporting Information). When seasonality in attenuation and sinking speed is present (Fig. 1(a)), the annual mean TE is no longer homogeneous and shows a broad spatial pattern of values ranging from approximately 0.15-0.3 in the Southern Ocean, North Atlantic and North Pacific, and 0.05-0.15 in the subtropical gyres and tropical areas. The consistent spatial pattern of high TE at high latitudes and low at low latitudes, particularly in the subtropics, is in agreement with previous attempts to estimate TE using a variety of methods such as data-constrained modelling [27, 28], large-scale mechanistic modelling [29] and from neutrally-buoyant sediment traps [26]. The exception is the pattern obtained from a deep-sea sediment and export fluxes compilation analysis [25, 35], which found TE to be higher in low latitudes than in high latitudes, which we will return to in the next section.

The annual mean TE in ocean provinces (Fig. 1(b); see Supporting Information for the provinces division and flux calculations) shows that the Antarctic province AAZ and North Atlantic province NA have high values of TE (0.18 and 0.16 respectively), while the subtropical provinces of STA and STP have the lowest values of 0.13 and 0.11 respectively, with all other provinces showing values in between. These estimates are in good qualitative agreement with previous modelling studies [29] and within the uncertainty margin of data-constrained modelling studies [27, 28] for all provinces but STP and NP in the Pacific Ocean, with the caveat that our province division is similar but slightly different (see Supporting Information). The annual global mean TE is 0.14, which also falls between the high and low latitude values in Fig. 1(a). However, it is slightly lower than the 0.15 given by the Martin curve when $b = 0.858$.

The emergence of a spatial pattern in TE in the model, despite having a spatially-homogeneous flux attenuation, is a direct consequence of the seasonal variability in the attenuation. If the attenuation is invariant throughout the year, its effect on the sinking detritus concentrations (and fluxes) is simply to reduce the concentration of detritus with depth, but keeping the shape of the time series unchanged (Fig. 2(a)), like a travelling wave under damping. Therefore, at different depths, the detritus concentration has the same seasonal cycle, but with an increasing lag relative to the export depth, as illustrated for a location in the South Atlantic in Fig. 2(c). Because this attenuation is constant at all locations, the ratio between the 1-year integral of the time series at any two depths below the export depth will be the same at any location (Fig. 2(a)). If seasonality is present, the differing attenuation at different times of the year will alter the time series of flux at depth, as periods of higher flux from the surface may coincide with low attenuation in some places and high attenuation in others. The deeper the depth horizon considered, the greater the lag with respect to the time series at the export depth, as shown in Fig. 2(b)and Fig. 2(d). As this distortion is dependent on the time series, the ratio between the 1-year integral of the time series at two depths below the export depth will be different at different locations. Examples of modelled time series in the Pacific and Indian Oceans are shown in Supporting Information.

Despite the clear link between seasonality and spatial variability, the above does not exclude the possibility of the existence of a background spatial trend in TE. Instead, our results demonstrate that annual spatial variability may not emerge uniquely from spatially-varying processes, such as temperature-dependent remineralisation, but could also arise from non-linear coupling between processes.

Reconciling previous studies

Our findings from the previous section are in agreement with those from several modelling and observation-based studies [26, 27, 28, 29], but at odds with estimates from a set of deep-ocean sediment trap and Thorium-derived export fluxes [25].

Previous suggestions [26] on how to reconcile these divergent estimates focused on the possibility of a fast upper mesopelagic attenuation followed by slow attenuation in the deep ocean in warm waters, with the converse happening in cold waters, but did not consider the role of seasonality and variability in flux attenuation and sinking speeds, nor the implicit steady-state assumption that is inherent in most reports of short-term observations of sinking POC [36]. Although this temperature-attenuation relationship was later observed in a data-constrained model analysis [28], the existence of this phenomenon was not enough to generate the high-latitude low-TE patterns [28].

Here we argue that the different time scales introduced by temporal variability of attenuation and sinking could provide an explanation for the high-latitude low-TE pattern. In a situation where flux attenuation and sinking speed vary seasonally, sufficiently frequent sampling to allow representation of global annual averages is not typically viable with ship-based observations. The existence of a seasonal cycle itself implies that if sampling the same location in the ocean at different times of the year, estimates of flux attenuation and TE are likely to be quite different. In addition, the

†Note that, after spinup, the cycle is quasi-periodic and not 100% periodic.

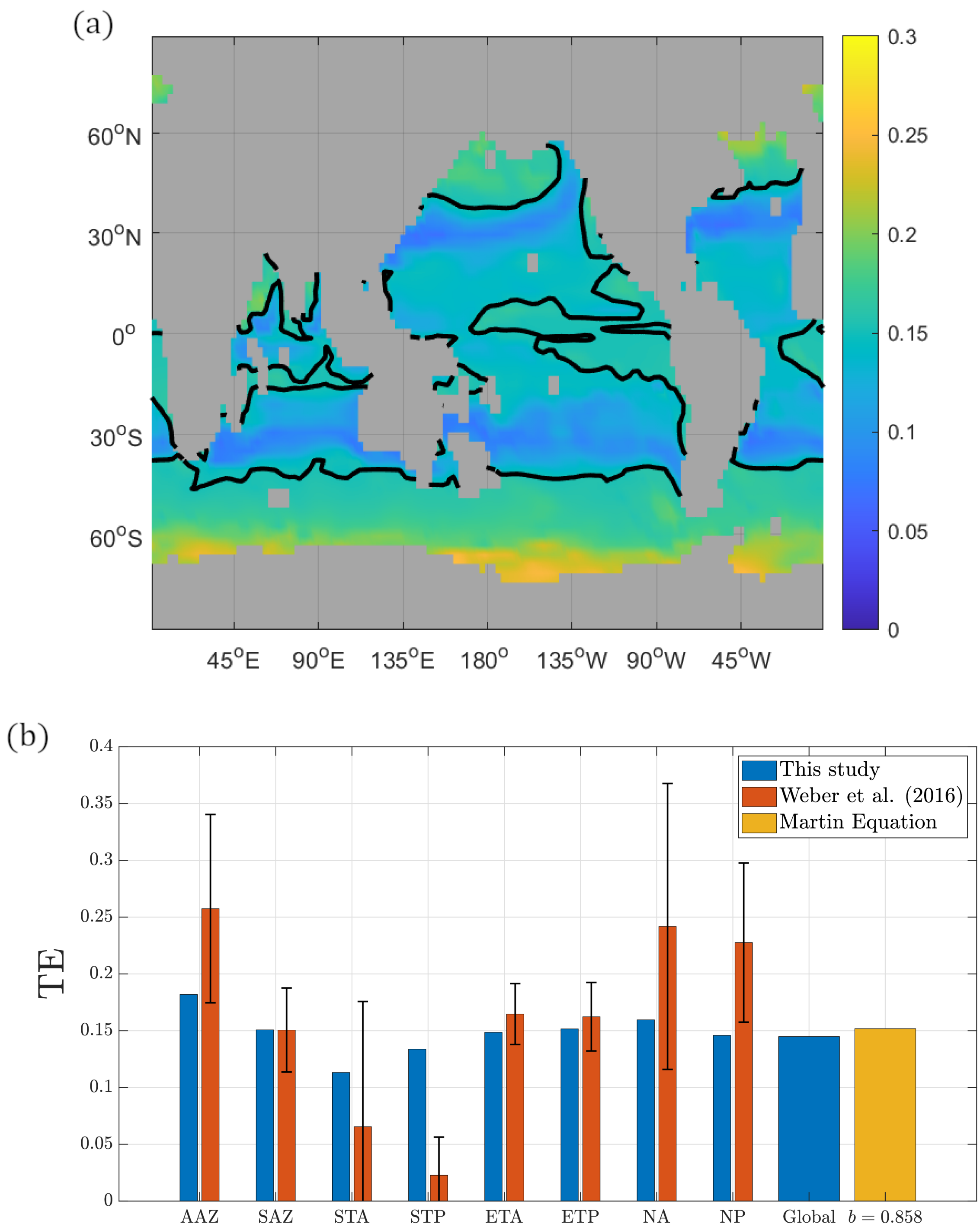

Figure 1: Annual mean transfer efficiency (TE), when detritus is not transported by the ocean circulation. Top: (a) TE for a seasonal b^{model} - the solid black contour lines represents the TE computed from the Martin curve for $b = 0.858$. Bottom: (b) annual mean TE in each ocean province (definition in the Supplementary Materials) using data from this study (blue bars) and the data-constrained modelling study [27] (red bars, with intervals indicating the uncertainty in their analysis), with the yellow bar showing the value for TE as estimated using the Martin curve (Supplementary Materials) for $b = 0.858$. Note that the province definition in this study and in the data-constrained modelling study [27] are slightly different (see Supplementary Materials).

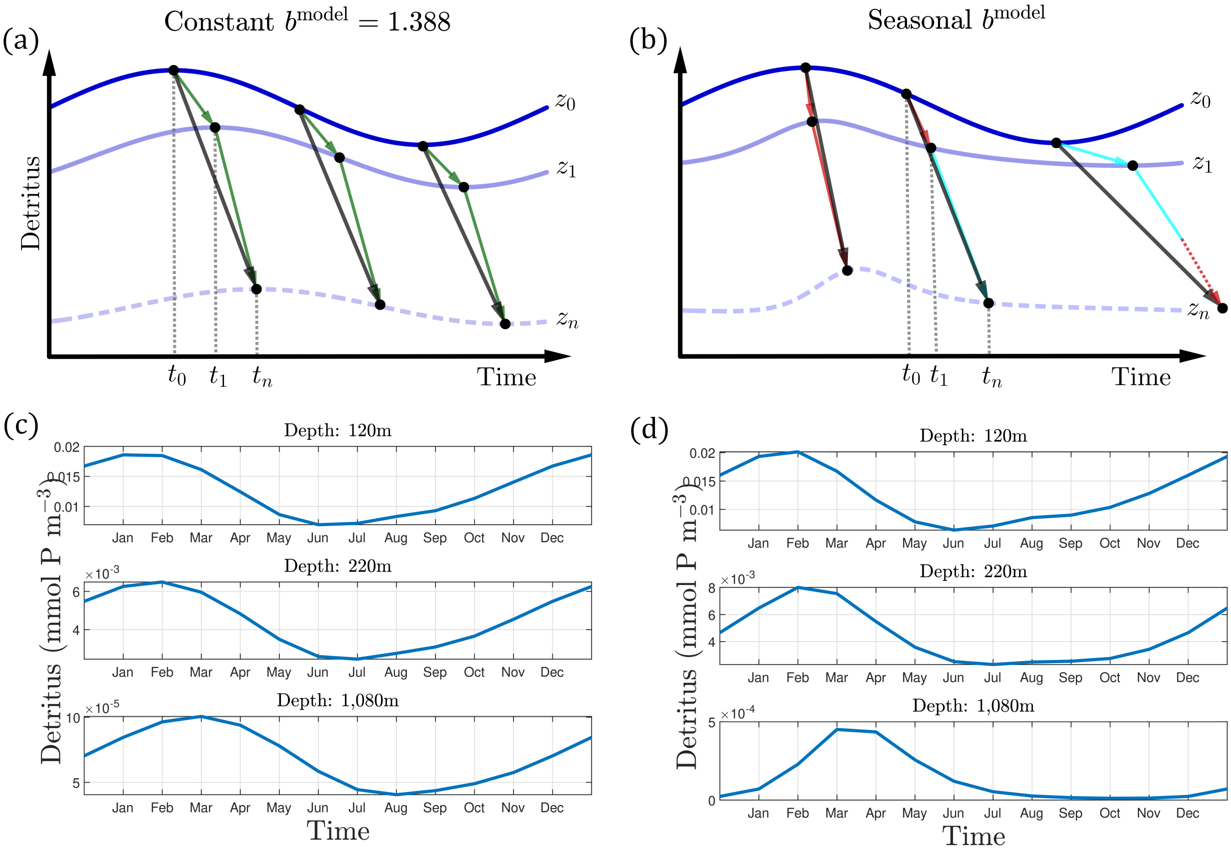

Figure 2: Exported detritus attenuation in constant and seasonal attenuation scenarios, when detritus is not transported by the ocean circulation. Top: schematic representation showing how detritus is attenuated in a non-seasonal scenario (a) and when seasonality is present (b). In (a), detritus that is at the export depth z_0 at an instant t_0 would be uniformly attenuated, reaching a depth z_1 at an instant t_1, as shown by the green arrow. Then, the attenuation continues at an uniform rate, with sinking speed increasing as a function of depth, so that the remaining detritus reaches the transfer depth z_n at an instant t_n. As both attenuation and sinking are constant in time, this process is independent of the starting point, as shown by the dark grey arrows, which are parallel to each other. In (b), the attenuation varies seasonally and hence the journey of detritus is dependent on time of the year. For instance, detritus that is at the export depth z_0 at the instant t_0 depicted would go through a lower attenuation, sinking at a faster rate until it reaches z_1 at the instant t_1, as shown by the red arrow. This is then followed by a faster attenuation, when detritus sinks at a slower rate, until it reaches the transfer depth z_n at an instant t_n, as shown by the light blue arrow. For detritus leaving z_0 at other times, the attenuation journey would be different, and hence the grey arrows are not parallel. Bottom: time series for detritus concentration in the South Atlantic (43.59°S, 29.53°W) at different depths for a constant $b^{\text{model}} = 1.388$ (c) and a seasonal b^{model} (d). Note the changing scale of the y-axes in panels (c) and (d).

seasonal cycle could be highly episodic: as ship-board observations are collected for very short periods, sampling might occur in e.g. an overall period of slow sinking with occasional short-lived peaks. Hence, compiling short duration observations from several years made at different times of the year and at different locations, might be misleading.

To test whether this mechanism could provide an answer to the contrasting patterns of TE reported by the Thorium-based study [25], we reproduced their sampling methodology as closely as possible from our model simulations, given the limitations of our modelling framework (see Supporting Information).

Fig. 3 shows the results of reproducing the Thorium-based study [25] using the same model data used to produce Fig. 1. Instead of computing the annual average export and transfer flux to produce a TE map as in Fig. 1(a), we sampled the model data at locations and times that best matched their approach (see Supporting Information for details). Specifically, we randomly sampled a total of 150 high and low latitude locations shown in Fig. 3(a), from which we took annual fluxes at 1,000m and seasonally averaged fluxes at 120m, with the corresponding mean upper-mesopelagic temperature (120m-540m) for the same period. We then used these data to compute TE at each sampled location, which was correlated (both linearly and exponentially, see Supplementary Materials) with the upper-mesopelagic mean temperature at the same location, as shown in Fig. 3(b). This process was repeated 10,000 times to quantify the uncertainty, giving a normally-distributed R^2 with mean 0.78 and variance 0.029 for the exponential regression (see Supplementary Materials). The mean correlation maps (linear and exponential) were then used to produce global TE maps. The resulting map for the exponential fit is shown in Fig. 3(b) (see Supplementary Materials for the linear fit map). Surprisingly, this provides a fairly reasonable explanation to the differences with the sediment trap-based study [26], showing a low TE in high latitudes and a higher TE in the tropics and subtropics, hence suggesting that the seasonal signal for export in these periods were enough to reverse the TE pattern from Fig. 1(a) - even though both TE maps were generated from the same data.

These results suggest that temporally-inconsistent data compilations could lead to differing conclusions, particularly when generalised to non-sampled parts of the ocean. In this case, measurements that have some consistency in time (i.e. from around the same time of the year) and location might be required to draw robust conclusions on the processes driving the biological carbon pump.

This study has some important limitations, including the use of a coarse resolution model which does not resolve small scale processes, as well as a periodically-repeating circulation. However, these methods have been successfully employed in a variety of studies [37, 38, 27, 28, 39]. Another limitation is in the use of a non-mechanistic seasonal cycle, which is based on very limited evidence [30, 31], and is nothing more than a minimal representation of seasonal variation in attenuation. In reality, it may vary in both amplitude and phase with location. The shape (i.e. how peaked) of the attenuation time series might, at some locations, be quite different from the simple profile (see Materials and Methods) considered in this work, and such a difference may also impact the results. In addition to that, the results in this study also ignore the effects, albeit small, of circulation in the transport of detritus, meaning that it can only move vertically due to gravity, but is not transported laterally. However, this is consistent with the data-constrained modelling study [27], which also assumed that the horizontal transport of detritus is negligible relative to the vertical sinking in their flux reconstruction. The coarse resolution also prevents a reproduction of the neutrally-buoyant sediment trap study [26], since their study corresponds to only 8 data points (4 North Atlantic, 4 North Pacific) which in our coarse-resolution model, roughly corresponds to only 4 locations. Among those, 3 North Atlantic locations near Iceland, and two locations near Japan are land points in our model, and hence we would have only 3 data points (averaged over a 2.8 degrees resolution cell) to work from, therefore compromising the statistical significance of the analysis.

These however do not affect the purpose of this study, which is not to reproduce reality *ipsis literis* but to test a hypothesis and demonstrate a phenomenon. Hence, despite being successful in reconciling previous literature results while highlighting an important but neglected phenomenon, it should not be taken as an intended accurate depiction of the real seasonal cycle, nor be reproduced in models as such. Note that it also ignores the fact that a real time series might show inter-annual variability, and hence its scope is limited to the hypothesis tested in this study.

Sampling, modelling and ways forward

How do we take into consideration the seasonal variability of sinking detritus and its attenuation to improve estimates of the biological carbon pump? A rather simplistic answer would be that measuring fluxes at many locations and depths and throughout the whole year for many years, and using this data to calibrate state-of-the-art ocean-biogeochemical models, may solve the issue. Unfortunately, such a large-scale, high-frequency sampling and optimisation approach would be costly and is logistically unfeasible in the near future, although BGC-Argo floats [40, 41] and derivative-free computational optimisers [42] offer some hope.

Instead, we argue that efforts should be put towards unravelling the mechanisms behind seasonal variability in the POC dynamics and incorporating it into models. This is of particular relevance for sinking speed as an important influence in POC attenuation, characterised by shifts between slow sinking particles (for which advection could be relevant and remineralisa-

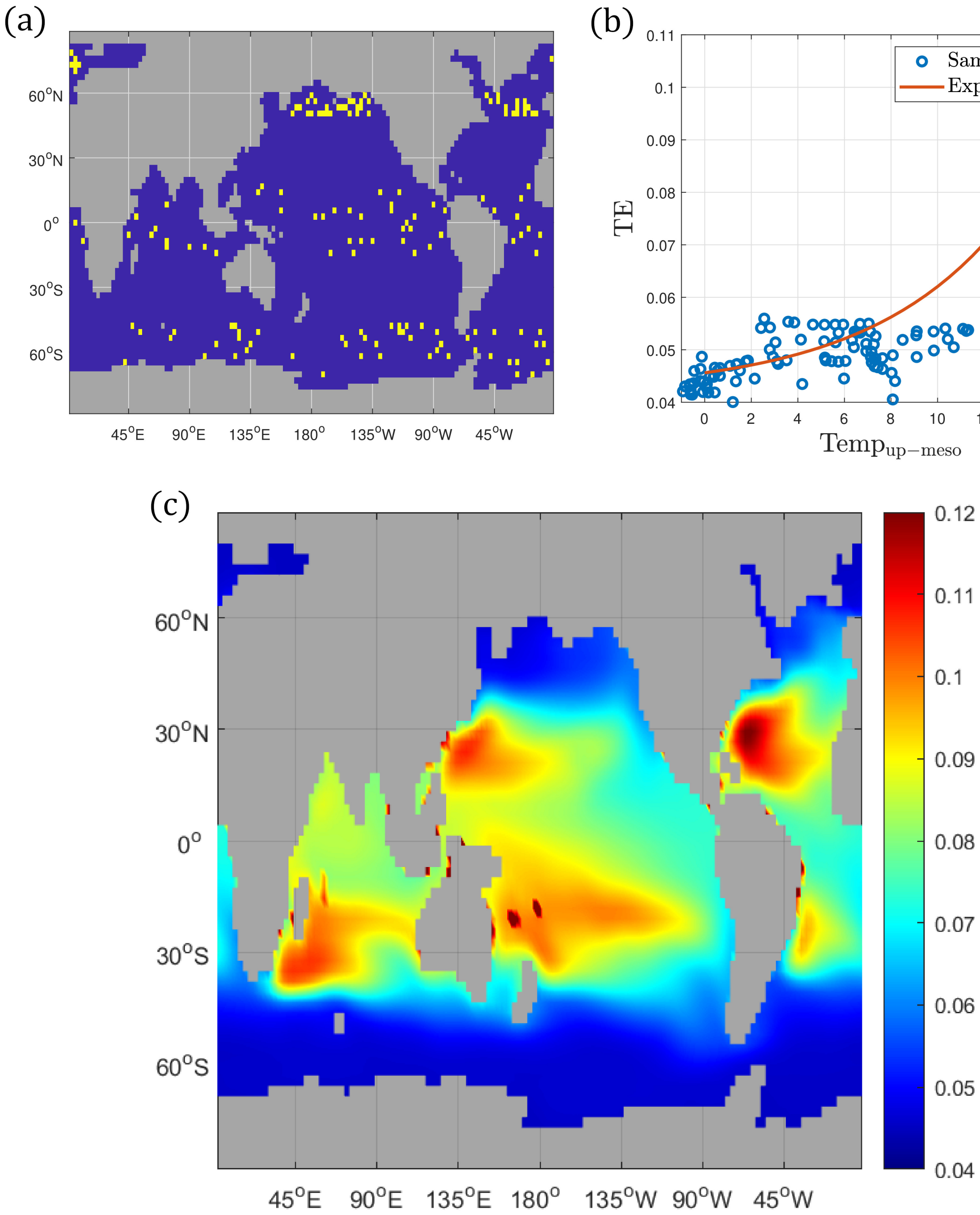

Figure 3: Annual mean TE computed from model data following the procedure in the thorium-based study [25]. Top: (a) export and transfer fluxes were sampled randomly, and (b) a nonlinear (exponential) regression of the resulting TE against the upper-mesopelagic temperature was performed. This procedure was repeated 10,000 times and the resulting parameterisation was used to compute the TE map shown in panel (c).

tion, aggregation and consumption takes place in the mesopelagic) and fast sinking particles (for which the influence of circulation is less relevant and gravity-driven movement dominates its dynamics). Therefore, a more realistic representation of the POC flux attenuation would likely be a dynamic, mechanistic one and likely to be dependent on other tracers, such as zooplankton (which can affect fragmentation [8]), oxygen [43] and possibly including bacteria and higher organisms such as fish - rather than being the smooth seasonal cycle used in the present study.

With that in mind, there are at least a couple of ways forward. The first is to elucidate the seasonal cycle using observations at different locations, at different depths and times. We believe that this could be achieved through use of both in-situ and remotely sensed data already available [41] (e.g. via data-constrained models [27, 28] or high-resolution data assimilation [44]), but also purposely designed fieldwork. Autonomous vehicles, which can collect high frequency data over months or years, and at several remote locations, will allow the seasonal cycle in particle flux to be constrained [45, 30] while reducing the (representation) error of using localised data as representative of large areas [46, 47] - which is an overlooked problem in ocean modelling, where single grid cells often represent areas of hundreds of kilometres. Controlled laboratory experiments may also be of help [16]. Alongside these efforts, the information gathered could support the derivation of robust mechanistic relationships between sinking, remineralisation, flux attenuation and other tracers and fields such as phytoplankton and zooplankton biomass, net primary production, temperature, upper-mesopelagic ocean circulation, and others.

This seasonal and mechanistic perspective has also important consequences for the understanding of the BCP under climate change. In fact, if one assumes that the sinking speed depends mechanistically on e.g. the ecosystem dynamics, one should expect that these cycles would vary seasonally but also inter-annually as the dynamics change due to anthropogenic forcing. Hence, for a robust understanding of the BCP under a transient climate, it is essential that we: 1) obtain direct measurements (or indirect estimates) of annual cycles at a suitable resolution (at least weekly to be comparable with high-turnover tracers such as phytoplankton); 2) elucidate leading order mechanisms behind variability in sinking speed and attenuation; 3) test any findings using computationally-affordable ocean-biogeochemical frameworks (such as the one used in this study); 4) whenever feasible, incorporate the findings in the next generation of IPCC models.

In this case, we note that most CMIP6 models adopt constant (in time, space and depth) sinking speed [33, 34], with only two models using a variable formulation: one has a sinking speed that is constant in time but increases with depth [48], and another has a sinking speed that varies according to the nutrient stress [49].

Summary and conclusion

In this paper we tested the hypothesis that seasonal variation in TE can explain spatial patterns that might otherwise result in biases in estimating the BCP. We showed that the addition of a seasonal cycle in the flux attenuation and sinking speed has at least three striking consequences for the global patterns of annual TE. First, spatial variability is generated despite both flux attenuation and sinking speed being spatially homogeneous at each instant of time. Second, the emerging spatial pattern in annual TE is highly similar to that reported in the literature [26, 27, 28, 29]. Third, accounting for the seasonality allows for the high-latitude high-TE map [26] to be reconciled with the Thorium-based high-latitude low-TE pattern [25].

These results suggest that seasonal variability in flux attenuation and sinking speed may be a route for generating spatial variability in annual TE, as a natural emerging property of the system dynamics. This is different from imposing a spatially-varying TE or b^{model} *a priori*, and is the simple consequence of the coupling between two nonlinear and seasonal time series (i.e. flux attenuation and export of organic material; or equivalently, sinking speed and detritus concentration) to obtain fluxes - excluding the transport due to circulation.

This has also implications for CMIP-class models run in a climate change scenario: changes in climate forcing might trigger changes in the seasonal cycle and hence impact spatial variability too. Hence, assuming a fixed spatial and temporal pattern in flux attenuation limits the model assessment of the BCP and sequestration under climate change in the IPCC scenarios. Currently, all CMIP models have invariant in time and space (and all but one have a constant in depth) sinking speed [33, 34], and incorporating mechanistic models for sinking particles is a challenge for the CMIP7 generation and beyond.

Finally, observationally resolving the temporal scales of fluxes and related processes such as sinking speed, remineralisation, and metabolic rates would represent a big step towards a better quantification and understanding of the BCP. Model estimates of flux are hard to validate due to sparsity of observations [27], not only spatially but especially temporally, but there is a potential for autonomous observations to fill in some of the gaps - particularly the seasonal variability [45, 30, 9, 41]. Even if such data are available, the computational costs to fit a model to it could be beyond computational capability for most complex models, given the number of degrees of freedom to be constrained. Use of data-constrained models and machine learning offer some hope and can be a fruitful avenue to extract information from the more abundant data existent for other tracers, and should be one of the top priorities for the biogeochemical modelling community over the next few years.

Materials and methods

Diagnostic model

We use a coupled global ocean-biogeochemical model. The biogeochemical component is the GEOMAR NPZD-DOP model [50, 51]. The biogeochemistry is coupled to the circulation via a transport-matrix (TMM) framework [52, 37, 53]. For the circulation, we use 12 monthly averaged transport matrices derived from the MITgcm 2.8° [52, 53]. This model includes detritus explicitly as a tracer, which sinks at an intrinsic speed $w(z) = a \cdot z$ m day^{-1}, $a > 0$, and is remineralised at a constant rate $\lambda = 0.05$ day^{-1}. In the absence of circulation, the 1-year average fluxes are given by the Martin curve, with $b = \lambda/a$. To avoid confusion with the Martin curve, we denote the model's flux attenuation by b^{model} [32]. With the TMM, it is also possible to easily turn off circulation influence on detritus, and hence remove its effect on detritus transport [32]. The latter is a crucial point in this study and, in all simulations, the ocean circulation does not act on the sinking detritus (but do act on all other tracers).

Seasonal cycle

The model has been modified to incorporate seasonality in its flux attenuation by modifying its sinking speed: since $a = \lambda/b^{\text{model}}$, we replace b^{model} by a seasonally-varying version with variability of 60% from the model's original reference value of $b^{\text{model}} = 1.388$, as shown in Fig. S1 (Supporting Information). This covers the range of observed values from about 0.5 to 2.0 [23]. The phase is chosen to be approximately 3 months ahead of growth and solar radiation (Supporting Information), and is within the uncertainty margin reported from annual sediment trap data for the North Red Sea [31]. The former means that fastest sinking (lowest attenuation and highest transfer efficiency) happens between February and May (as suggested by North Atlantic glider data [30]), which occurs 3 months after maximum growth. Note that the seasonal b^{model} spatially homogeneous at each instant of time, so there is no spatial variability in b^{model} or in sinking speed at each depth.

Model data

All model output used in this work is freely available online on Zenodo [54]. The data [27] used to generate Fig. 1(b) is available on Bitbucket [29, 55]. All figures in this work were generated by the authors, except the aforementioned Fig. 1(b), which includes data from the data-constrained modelling study [27] published by others [29]. Fig. 2(a) and Fig. 2(b) were generated using the software GeoGebra [56].

Acknowledgements

This work was funded by: an European Research Council Consolidator grant (GOCART, agreement number 724416) in support of F.d.M.V. and S.A.H.; by a Large Grant from the UK Natural Environment Research Council (COMICS, agreement numbers NE/M020835/1 and NE/M020835/2) in support of F.d.M.V., A.P.M. and S.A.H.; and by a UK Natural Environment Research Council RoSES programme grant (CUSTARD, agreement number NE/P021247/2) in support of F.d.M.V., A.P.M. and S.A.H. J.D.W. acknowledges support from the AXA Research Fund.

References

[1] Tyler Volk and Martin I. Hoffert. *Ocean Carbon Pumps: Analysis of Relative Strengths and Efficiencies in Ocean-Driven Atmospheric CO2 Changes*, pages 99–110. American Geophysical Union (AGU), 2013.

[2] I. D. Lima, P. J. Lam, and S. C. Doney. Dynamics of particulate organic carbon flux in a global ocean model. *Biogeosciences*, 11(4):1177–1198, 2014.

[3] Grace K. Saba, Adrian B. Burd, John P. Dunne, Santiago Hernández-León, Angela H. Martin, Kenneth A. Rose, Joseph Salisbury, Deborah K. Steinberg, Clive N. Trueman, Rod W. Wilson, and Stephanie E. Wilson. Toward a better understanding of fish-based contribution to ocean carbon flux. *Limnology and Oceanography*, 66(5):1639–1664, 2021.

[4] Tim DeVries, Francois Primeau, and Curtis Deutsch. The sequestration efficiency of the biological pump. *Geophysical Research Letters*, 39(13), 2012.

[5] E. Maier-Reimer, U. Mikolajewicz, and A. Winguth. Future ocean uptake of CO_2: interaction between ocean circulation and biology. *Climate Dynamics*, 12:711–722, 1996.

[6] Roger Francois, Susumu Honjo, Richard Krishfield, and Steve Manganini. Factors controlling the flux of organic carbon to the bathypelagic zone of the ocean. *Global Biogeochemical Cycles*, 16(4):34–1–34–20, 2002.

[7] A. Riazi, A. Vila-Concejo, T. Salles, and U. Türker. Improved drag coefficient and settling velocity for carbonate sands. *Scientific Reports*, 10:9465, 2020.

[8] Daniel J. Mayor, Wendy C. Gentleman, and Thomas R. Anderson. Ocean carbon sequestration: Particle fragmentation by copepods as a significant unrecognised factor? *BioEssays*, 42(12):2000149, 2020.

[9] Nathan Briggs, Giorgio Dall'Olmo, and Hervé Claustre. Major role of particle fragmentation in regulating biological sequestration of CO_2 by the oceans. *Science*, 367(6479):791–793, 2020.

[10] Robert A. Armstrong, Cindy Lee, John I. Hedges, Susumu Honjo, and Stuart G. Wakeham. A new, mechanistic model for organic carbon fluxes in the ocean based on the quantitative association of poc with ballast minerals. *Deep Sea Research Part II: Topical Studies in Oceanography*, 49(1):219 – 236, 2001. The US JGOFS Synthesis and Modeling Project: Phase 1.

[11] Christine Klaas and David E. Archer. Association of sinking organic matter with various types of mineral ballast in the deep sea: Implications for the rain ratio. *Global Biogeochemical Cycles*, 16(4):63–1–63–14, 2002.

[12] Emily J. Zakem and Naomi M. Levine. Systematic variation in marine dissolved organic matter stoichiometry and remineralization ratios as a function of lability. *Global Biogeochemical Cycles*, n/a(n/a), 2019.

[13] Philip Boyd and Fraser Kennedy. Microbes in a sea of sinking particles. *Nature Microbiology*, 6:1–2, 11 2021.

[14] N. Arandia-Gorostidi, H. Berthelot, F. Calabrese, H. Stryhanyuk, I Klawonn, M. Iversen, N. Nahar, H-P. Grossart, H. Ploug, and N. Musat. Efficient carbon and nitrogen transfer from marine diatom aggregates to colonizing bacterial groups. *Scientific Reports*, 12:14949, 2022.

[15] F. Boscolo-Galazzo, K.A. Crichton, S. Barker, and P.N. Pearson. Temperature dependency of metabolic rates in the upper ocean: A positive feedback to global climate change? *Global and Planetary Change*, 170:201–212, 2018.

[16] U. Alcolombri, F.J. Peaudecerf, V.I. Fernandez, L. Behrendt, K. Soo Lee, and R. Stocker. Sinking enhances the degradation of organic particles by marine bacteria. *Nature Geosciences*, 14:775–780, 2021.

[17] John H. Martin, George A. Knauer, David M. Karl, and William W. Broenkow. Vertex: carbon cycling in the northeast pacific. *Deep Sea Research Part A. Oceanographic Research Papers*, 34(2):267 – 285, 1987.

[18] Jack J. Middelburg. *Marine Carbon Biogeochemistry: A Primer for Earth System Scientists*. Springer International Publishing, 1st edition, 2019.

[19] William M. Berelson. The flux of particulate organic carbon into the ocean interior: A comparison of four u.s. jgofs regional studies. *Oceanography*, 14:59–67, 2001.

[20] Ken O. Buesseler, Carl H. Lamborg, Philip W. Boyd, Phoebe J. Lam, Thomas W. Trull, Robert R. Bidigare, James K. B. Bishop, Karen L. Casciotti, Frank Dehairs, Marc Elskens, Makio Honda, David M. Karl, David A. Siegel, Mary W. Silver, Deborah K. Steinberg, Jim Valdes, Benjamin Van Mooy, and Stephanie Wilson. Revisiting carbon flux through the ocean's twilight zone. *Science*, 316(5824):567–570, 2007.

[21] Maureen H Conte, Nate Ralph, and Edith H Ross. Seasonal and interannual variability in deep ocean particle fluxes at the oceanic flux program (ofp)/bermuda atlantic time series (bats) site in the western sargasso sea near bermuda. *Deep Sea Research Part II: Topical Studies in Oceanography*, 48(8):1471–1505, 2001.

[22] Michael Lutz, Robert Dunbar, and Ken Caldeira. Regional variability in the vertical flux of particulate organic carbon in the ocean interior. *Global Biogeochemical Cycles*, 16(3):11–1–11–18, 2002.

[23] E. Kwon, F. Primeau, and J. Sarmiento. The impact of remineralization depth on the air–sea carbon balance. *Nature Geosciences*, 2:630–635, 2009.

[24] J. D. Wilson, S. Barker, N. R. Edwards, P. B. Holden, and A. Ridgwell. Sensitivity of atmospheric co2 to regional variability in particulate organic matter remineralization depths. *Biogeosciences*, 16(14):2923–2936, 2019.

[25] Stephanie A. Henson, Richard Sanders, and Esben Madsen. Global patterns in efficiency of particulate organic carbon export and transfer to the deep ocean. *Global Biogeochemical Cycles*, 26(1), 2012.

[26] Chris M. Marsay, Richard J. Sanders, Stephanie A. Henson, Katsiaryna Pabortsava, Eric P. Achterberg, and Richard S. Lampitt. Attenuation of sinking particulate organic carbon flux through the mesopelagic ocean. *Proceedings of the National Academy of Sciences*, 112(4):1089–1094, 2015.

[27] Thomas Weber, Jacob A. Cram, Shirley W. Leung, Timothy DeVries, and Curtis Deutsch. Deep ocean nutrients imply large latitudinal variation in particle transfer efficiency. *Proceedings of the National Academy of Sciences*, 113(31):8606–8611, 2016.

[28] Tim DeVries and Thomas Weber. The export and fate of organic matter in the ocean: New constraints from combining satellite and oceanographic tracer observations. *Global Biogeochemical Cycles*, 31(3):535–555, 2017.

[29] Jacob A. Cram, Thomas Weber, Shirley W. Leung, Andrew M. P. McDonnell, Jun-Hong Liang, and Curtis Deutsch. The role of particle size, ballast, temperature, and oxygen in the sinking flux to the deep sea. *Global Biogeochemical Cycles*, 32(5):858–876, 2018.

[30] Roséanne Bol, Stephanie A. Henson, Anna Rumyantseva, and Nathan Briggs. High-frequency variability of small-particle carbon export flux in the northeast atlantic. *Global Biogeochemical Cycles*, 32(12):1803–1814, 2018.

[31] Stephanie. S. Kienast and Adi Torfstein. Evaluation of biological carbon pump metrics in the subtropical gulf of aqaba, northern red sea. *Global Biogeochemical Cycles*, 36(10):e2022GB007452, 2022. e2022GB007452 2022GB007452.

[32] Francisco de Melo Viríssimo, Adrian P. Martin, and Stephanie A. Henson. Influence of seasonal variability in flux attenuation on global organic carbon fluxes and nutrient distributions. *Global Biogeochemical Cycles*, 36(2):e2021GB007101, 2022.

[33] S.A. Henson, C. Laufkötter, S. Leung, S.L.C. Giering, H.I. Palevski, and E.L. Cavan. Uncertain response of ocean biological carbon export in a changing world. *Nature Geosciences*, 15:248–254, 2022.

[34] Jamie D. Wilson, Oliver Andrews, Anna Katavouta, Francisco de Melo Viríssimo, Ros M. Death, Markus Adloff, Chelsey A. Baker, Benedict Blackledge, Fraser W. Goldsworth, Alan T. Kennedy-Asser, Qian Liu, Katie R. Sieradzan, Emily Vosper, and Rui Ying. The biological carbon pump in cmip6 models: 21st century trends and uncertainties. *Proceedings of the National Academy of Sciences*, 119(29):e2204369119, 2022.

[35] Lionel Guidi, Louis Legendre, Gabriel Reygondeau, Julia Uitz, Lars Stemmann, and Stephanie A. Henson. A new look at ocean carbon remineralization for estimating deepwater sequestration. *Global Biogeochemical Cycles*, 29(7):1044–1059, 2015.

[36] Sarah L. C. Giering, Richard Sanders, Adrian P. Martin, Stephanie A. Henson, Jennifer S. Riley, Chris M. Marsay, and David G. Johns. Particle flux in the oceans: Challenging the steady state assumption. *Global Biogeochemical Cycles*, 31(1):159–171, 2017.

[37] Samar Khatiwala. A computational framework for simulation of biogeochemical tracers in the ocean. *Global Biogeochemical Cycles*, 21(3), 2007.

[38] I. Kriest and A. Oschlies. Swept under the carpet: organic matter burial decreases global ocean biogeochemical model sensitivity to remineralization length scale. *Biogeosciences*, 10(12):8401–8422, 2013.

[39] D. Niemeyer, I. Kriest, and A. Oschlies. The effect of marine aggregate parameterisations on nutrients and oxygen minimum zones in a global biogeochemical model. *Biogeosciences*, 16(15):3095–3111, 2019.

[40] Hervé Claustre, Kenneth S. Johnson, and Yuichiro Takeshita. Observing the global ocean with biogeochemical-argo. *Annual Review of Marine Science*, 12(1):23–48, 2020. PMID: 31433959.

[41] Robert J.W. Brewin, Shubha Sathyendranath, Trevor Platt, Heather Bouman, Stefano Ciavatta, Giorgio Dall'Olmo, James Dingle, Steve Groom, Bror Jönsson, Tihomir S. Kostadinov, Gemma Kulk, Marko Laine, Victor Martínez-Vicente, Stella Psarra, Dionysios E. Raitsos, Katherine Richardson, Marie-Hélène Rio, Cécile S. Rousseaux, Joe Salisbury, Jamie D. Shutler, and Peter Walker. Sensing the ocean biological carbon pump from space: A review of capabilities, concepts, research gaps and future developments. *Earth-Science Reviews*, 217:103604, 2021.

[42] S. Oliver, C. Cartis, I. Kriest, S. F. B. Tett, and S. Khatiwala. A derivative-free optimisation method for global ocean biogeochemical models. *Geoscientific Model Development*, 15(9):3537–3554, 2022.

[43] E. Cavan, M. Trimmer, F. Shelley, and R. Sanders. Remineralization of particulate organic carbon in an ocean oxygen minimum zone. *Nature Communications*, 8(14847):1–9, 2017.

[44] S. Barthélémy, J. Brajard, L. Bertino, and F. Counillon. Super-resolution data assimilation. *Ocean Dynamics*, 72:661–678, 2022.

[45] Giorgio Dall'Olmo and Kjell Arne Mork. Carbon export by small particles in the norwegian sea. *Geophysical Research Letters*, 41(8):2921–2927, 2014.

[46] Peter R. Oke and Pavel Sakov. Representation error of oceanic observations for data assimilation. *Journal of Atmospheric and Oceanic Technology*, 25(6):1004 – 1017, 2008.

[47] D. Hodyss and N. Nichols. The error of representation: basic understanding. *Tellus A: Dynamic Meteorology and Oceanography*, 67(1):24822, 2015.

[48] O. Aumont, C. Ethé, A. Tagliabue, L. Bopp, and M. Gehlen. Pisces-v2: an ocean biogeochemical model for carbon and ecosystem studies. *Geoscientific Model Development*, 8(8):2465–2513, 2015.

[49] M. Vichi, N. Pinardi, and S. Masina. A generalized model of pelagic biogeochemistry for the global ocean ecosystem. part i: Theory. *Journal of Marine Systems*, 64(1):89–109, 2007. Contributions from Advances in Marine Ecosystem Modelling Research, 27-29 June, 2005, Plymouth, UK.

[50] I. Kriest, S. Khatiwala, and A. Oschlies. Towards an assessment of simple global marine biogeochemical models of different complexity. *Progress in Oceanography*, 86(3):337 – 360, 2010.

[51] I. Kriest, A. Oschlies, and S. Khatiwala. Sensitivity analysis of simple global marine biogeochemical models. *Global Biogeochemical Cycles*, 26(2), 2012.

[52] Samar Khatiwala, Martin Visbeck, and Mark A. Cane. Accelerated simulation of passive tracers in ocean circulation models. *Ocean Modelling*, 9(1):51 – 69, 2005.

[53] Samar Khatiwala. samarkhatiwala/tmm: Version 2.0 of the transport matrix method software (2018, may 13). *Zenodo*, 2018.

[54] Francisco de Melo Viríssimo, Adrian P. Martin, Stephanie A. Henson, and Jamie D. Wilson. Model output used in the manuscript "Seasonal variability in particle flux attenuation in the global ocean generates spatial variability in annual transfer efficiency" (v1.0). *Zenodo*, 2023.

[55] Jacob A. Cram. Model output used in the manuscript "the role of particle size, ballast, temperature, and oxygen in the sinking flux to the deep sea". `https://bitbucket.org/ohnoplus/prism-transfer-efficiency`, 2018. Last checked on 08.01.2023.

[56] M. Hohenwarter, M. Borcherds, G. Ancsin, B. Bencze, M. Blossier, J. Éliás, K. Frank, L. Gál, A. Hofstätter, F. Jordan, Z. Konečný, Z. Kovács, E. Lettner, S. Lizelfelner, B. Parisse, C. Solyom-Gecse, C. Stadlbauer, and M. Tomaschko. GeoGebra 5.0.507.0, October 2018. `http://www.geogebra.org`.

SUPPLEMENTARY MATERIALS

SEASONAL VARIABILITY IN PARTICLE FLUX ATTENUATION IN THE GLOBAL OCEAN GENERATES SPATIAL VARIABILITY IN ANNUAL TRANSFER EFFICIENCY

F. DE MELO VIRÍSSIMO[1,2,*], A. P. MARTIN[1], S. A. HENSON[1], J. D. WILSON[3,4]

[1] *National Oceanography Centre, Southampton, SO14 3ZH, United Kingdom*
[2] *Grantham Research Institute on Climate Change and the Environment, London School of Economics and Political Science, London, WC2A 2AE, United Kingdom*
[3] *School of Earth Sciences, University of Bristol, Bristol, BS8 1QU, United Kingdom*
[4] *Department of Earth, Ocean and Ecological Sciences, University of Liverpool, Liverpool, L69 3GP, United Kingdom*

NOTE: THIS IS A NON-PEER REVIEWED PREPRINT SUBMITTED TO EARTHARXIV

This PDF file includes:

- **Supplementary text**
- **Figures S.1 to S.14**
- **Tables S.1 to S.2**
- **SI References**

*Corresponding Author. e-mail: f.de-melo-virissimo@lse.ac.uk.

1 Diagnostic model

The diagnostic model [1, 2] used in this study has been modified to include a seasonal cycle in the model's flux attenuation and sinking speed coefficient, which we denote by b^{model} and a (day^{-1}) respectively - the latter making the sinking speed as $w(z) = a \cdot z$ (m day^{-1}). This change alters the sinking speed such that $a = \lambda / b^{\text{model}}$ [1, 3] (see also Equations (2.4), (3.4) and (3.5) below).

The seasonal b^{model} is presented in Fig. S.1 and is mathematically given by

$$b^{\text{model}}(t, \phi) = 1.388 + \text{sign}(\phi) \cdot 0.6 \cdot \cos\left(2 \cdot \pi \cdot (t/T) + (\theta \cdot \pi/6)\right) \tag{1.1}$$

There, t corresponds to the time (in days) and $T = 360$ days. The number 1.388 corresponds to the optimal, original b^{model} in which the model is normally run. The value 0.6 is chosen so that b^{model} goes from about 0.5 to just above 2.0 across the year, therefore covering the range of observation-derived values reported in the literature [4]. The phase is chosen to be $\theta = 3$ months [5, 6], so that faster sinking (low attenuation) happens about 3 months after maximum growth as indicated in Fig. S.1(c). The variable ϕ corresponds to the latitude, which varies from -90° to 90°. Hence, the signal function sign(ϕ) is positive in the Northern Hemisphere and Negative in the South. This means that, at each instant of time, the seasonal cycle is spatially homogeneous in each hemisphere.

The biogeochemical model is coupled to an offline version of the MITgcm 2.8° via the transport-matrix method (TMM) [7, 8, 9]. In addition to the well known advantages of using the TMM, this coupling allows one to easily turn off the circulation contribution to the detritus dynamics, which in turn is necessary to properly assess the influence of seasonality in transfer efficiency, as well as to compare our results with those obtained in the data-constrained modelling study [10].

All figures shown in this Supporting Information were generated from the model output available on Zenodo [11].

1.1 Detritus modelling

Below the export zone z_0 (in this model set as z_0 =120m), the detritus pool is modelled as a passive tracer according to the following equation [1]

$$\frac{\partial}{\partial t} C(x, y, z, t) = \text{circulation} + \text{sinking} + \text{remineralisation}, \tag{1.2}$$

where $C(x, y, z, t)$ is the detritus concentration at a point (x, y, z) in space and at an instant t in time (days).

While the circulation component in Equation (1.2) is given by an advection-diffusion equation (plus eddy parameterisations) [12] that have been stored as a series of 12 transport matrices [7], both sinking and remineralisation components are modelled as below, following [1]:

$$\text{sinking} = \frac{\partial}{\partial z} \left(w(z) \cdot C(x, y, z, t) \right),$$

where $w(z)$ is the sinking speed (m day^{-1}),

$$\text{remineralisation} = -\left(\lambda \cdot C(x, y, z, t) \right).$$

where λ is the remineralisation rate (day^{-1}).

This leads to the following equation

$$\frac{\partial}{\partial t} C(x, y, z, t) = \text{circulation} + \frac{\partial}{\partial z} \left(w(z) \cdot C(x, y, z, t) \right) - \left(\lambda \cdot C(x, y, z, t) \right), \tag{1.3}$$

which is the general equation for detritus in this model [1].

1.2 Spinup and analytical solution

The model was spun up for 3,000 years to reach a consistently quasi-repeating annual cycle, a procedure that is consistent with the literature [1]. This means that, if C is the solution, then $C(x, y, z, t) = C(x, y, z, t + T)$, for any $t > 0$ after the model has been spun up, where the 1-year period in this model is given by $T = 360$ days. Hence,

$$\int_0^T \frac{\partial}{\partial t} C(x, y, z, t) dt = C(x, y, z, T) - C(x, y, z, 0) = 0, \tag{1.4}$$

Note that, in general $\frac{\partial}{\partial t} C(x, y, z, t) \neq 0$ as the concentration is not stationary after (or during) spinup (as shown in previous studies [3]). The relationship above shows that it is the annual average after spinup that is stationary.

From the above, we are able to derive an analytical solution for the detritus concentration. If we ignore the circulation component and integrate both sides of Equation (1.3) over 1-year period T, the left-hand side will be zero, while the right-hand side will lead to an ordinary differential equation (ODE) to give $\overline{C}$. This can be solved analytically and the solution will be given by the Martin curve (see Equation (3.4)).

2 Revisiting particle flux and transfer efficiency

The POC transport at a location is usually quantified in terms of its molar flux F, which is given by the number of moles per unit time per unit area. Mathematically, we have

$$F(x, y, z, t) = w(z) \cdot C(x, y, z, t), \tag{2.1}$$

where C and w are the POC concentration and sinking speed, respectively. From now on, we shall omit the independent variables x and y (latitude and longitude, respectively) for simplicity, since all the analyses here are on depth z and time t.

The annual transfer efficiency TE, from the export depth z_0 to a depth $z > z_0$, is given by

$$\mathrm{TE} = \frac{\overline{F(z, t)}}{\overline{F(z_0, t)}}, \tag{2.2}$$

where the overline denotes the 1-year average.

2.1 Seasonality as a source of spatial variability

If the sinking speed w does not depend on time, then

$$\overline{F(z, t)} = \left(\frac{1}{T}\right) \int_0^T w(z) \cdot C(z, t) dt = w(z) \cdot \left(\frac{1}{T}\right) \int_0^T C(z, t) dt = w(z) \cdot \overline{C(z, t)}. \tag{2.3}$$

meaning that the sinking speed and concentration are essentially decoupled in time. In other words, the mean of the product equals the product of the means.

In the absence of circulation, this implies in an analytical solution to the flux of detritus and TE. In fact, ignoring circulation leads to

$$\frac{\partial}{\partial t} C(x, y, z, t) = \frac{\partial}{\partial z} \left(w(z) \cdot C(x, y, z, t)\right) - \left(\lambda \cdot C(x, y, z, t)\right),$$

If we integrate both sides of this equation over 1-year period T, we get

$$C(x, y, z, T) - C(x, y, z, 0) = \frac{\partial}{\partial z} \left(w(z) \cdot \overline{C}(x, y, z, t)\right) - \left(\lambda \cdot \overline{C}(x, y, z, t)\right),$$

which combined with Equation (1.4) gives

$$\frac{\partial}{\partial z} \left(w(z) \cdot \overline{C}(x, y, z, t)\right) - \left(\lambda \cdot \overline{C}(x, y, z, t)\right) = 0.$$

The equation above can be rewritten as an ODE in z for $\overline{C}$, which has an analytical solution given by the Martin curve (see Equation (3.4)). Hence (see also Equation (3.5)),

$$\mathrm{TE} = \frac{\overline{F(z, t)}}{\overline{F(z_0, t)}} = \frac{w(z) \cdot \overline{C(z, t)}}{w(z_0) \cdot \overline{C(z_0, t)}} = \left(\frac{z}{z_0}\right)^{-\lambda/a}. \tag{2.4}$$

Therefore, in the absence of circulation, the annual mean TE should be constant throughout the ocean, with the value given by Equation (2.4). This is illustrated in Fig. S.2 for the model's $-\lambda/a = b^{\mathrm{model}} = 1.388$, where the export depth $z_0 = 120$m and the transfer depth $z =$1,080m. In these conditions, Equation (2.4) gives TE≈ 0.04738, in very good agreement with Fig. S.2.

The same does not happen if a (and hence the sinking speed) varies seasonally. In fact, if we suppose that $a = a(t)$, then $w = w(z, t) = a(t) \cdot z$ and hence the sinking speed cannot be taken out of the time-average integral in Equation (2.3). In other words, if w does depend on time, then

$$\overline{F(z, t)} = \left(\frac{1}{T}\right) \int_0^T w(z, t) \cdot C(z, t) dt = \overline{w(z, t) \cdot C(z, t)} \neq \overline{w(z, t)} \cdot \overline{C(z, t)}, \tag{2.5}$$

and the relationship in Equation (2.4) does not hold for $a = a(t)$.

This coupling between seasonality in sinking speed and seasonality in detritus concentration implies that, at each point in space (due to spatial variability in detritus concentration) and depth (due to the variability in time of the already sinking detritus), a different time series with different annual mean will emerge, hence leading to spatial variability in the flux ratios - and in particular in TE.

2.2 Examples

Examples illustrating the influence of seasonality in the detritus concentration and fluxes are provided in Fig. S.3 to Fig. S.7 for the South Atlantic, North Atlantic, South Pacific, North Pacific and Indian oceans, respectively. Fig.S.3(a) and Fig. S.3(b) are also shown in the main manuscript as Fig. 2(c) and Fig. 2(d), respectively.

3 Metrics computed

The local transfer efficiency TE at a point latitude x and longitude y is defined as

$$\mathrm{TE}(x,y) = \frac{\overline{F}(x,y,z=1,080\mathrm{m})}{\overline{F}(x,y,z=120\mathrm{m})}. \tag{3.1}$$

The globally-integrated flux at a depth $z = z^*\mathrm{m}$ is given by

$$F_{z^*\mathrm{m}} = \int_{(x,y)} \overline{F}(x,y,z=z^*\mathrm{m})dxdy. \tag{3.2}$$

The global transfer efficiency can be computed as

$$\mathrm{TE}_{\mathrm{global}} = \frac{F_{1,080\mathrm{m}}}{F_{120\mathrm{m}}}, \tag{3.3}$$

where the export and transfer depth values of $z = 120$m and $z = 1,080$m respectively are imposed by the model as the depths where the diagnostic fluxes are evaluated.

Martin curve is given by

$$\overline{F}(x,y,z) = \overline{F}(x,y,z=z_0)\cdot\left(\frac{z}{z_0}\right)^{-b}, \tag{3.4}$$

where b is the flux attenuation parameter. In the conditions of Equation (2.3) and Equation (2.4), we have that $b = \lambda/a$.

From the Martin curve above, it follows that

$$\mathrm{TE} = \frac{\overline{F}(x,y,z=1,080\mathrm{m})}{\overline{F}(x,y,120\mathrm{m})} = \left(\frac{z=1,080\mathrm{m}}{z=120\mathrm{m}}\right)^{-b}. \tag{3.5}$$

3.1 Mean temperature

Here we consider the annual mean of the upper-mesopelagic (120-540m) ocean temperature. This average takes in consideration the relative volume of each grid box and can be computed as

$$\mathrm{Temp}_{\mathrm{up-meso}}(x,y) = \left(\frac{1}{\mathrm{Vol}_{\mathrm{up-meso}}(x,y)}\right)\int_{z=120\mathrm{m}}^{z=540\mathrm{m}} \overline{\mathrm{Temp}}(x,y,z)dz, \tag{3.6}$$

where $\overline{\mathrm{Temp}}(x,y,z)$ is the 1-year ocean mean temperature and

$$\mathrm{Vol}_{\mathrm{up-meso}}(x,y) = \int_{z=120\mathrm{m}}^{z=540\mathrm{m}} \mathrm{Vol}(x,y,z)dz \tag{3.7}$$

is the volume of the upper-mesopelagic water column at each point (x,y), with $\mathrm{Vol}(x,y,z)$ being the volume of the grid box located at (x,y,z).

3.2 Provinces division

The division of the ocean in zones (or provinces) used here is similar to that adopted in previous studies [10] and is based on the annual mean of the upper-mesopelagic ocean temperature as main indicator, as well as latitude and longitude. The division is described below, and the result is shown in Fig. S.8. Note that the latitude and longitude differs from the label in Fig. S.8: in the description, the latitude ranges from $-90°$ (corresponding to 90° South) to 90° (corresponding to 90° North) and the longitude ranges from 0° (corresponding to the Greenwich Meridian) eastward to 360°. This due to the data being labelled that way.

- Antactic Zone (AAZ): $\mathrm{Temp}_{\mathrm{up-meso}}(x,y) < 4$ and Latitude $< -45°$.
- Subantarctic Zone (SAZ): $4 \leq \mathrm{Temp}_{\mathrm{up-meso}}(x,y) < 13.5$ and Latitude $< -35°$.

- North Pacific (NP): $4 \leq \text{Temp}_{\text{up-meso}}(x,y) < 13.5$ and Latitude $> 25°$ and Longitude $< 280°$.
- North Atlantic (NA): $-10 \leq \text{Temp}_{\text{up-meso}}(x,y) < 13.5$ and Latitude $> 25°$ and Longitude $< 100°$ and Longitude $> 250°$.
- Eastern Tropical Atlantic (ETA): $4 \leq \text{Temp}_{\text{up-meso}}(x,y) < 13.5$ and $-35° <$ Latitude $< 25°$ and Longitude $< 50°$ and Longitude $> 300°$.
- Eastern Tropical Pacific (ETP): $4 \leq \text{Temp}_{\text{up-meso}}(x,y) < 13.5$ and $-35° <$ Latitude $< 25°$ and $50° <$ Longitude $< 300°$.
- Subtropical Pacific (STP): $\text{Temp}_{\text{up-meso}}(x,y) \geq 13.5$ and Longitude $< 274.2°$.
- Subtropical Atlantic (STA): $\text{Temp}_{\text{up-meso}}(x,y) \geq 13.5$ and Longitude $> 274.2°$.

3.3 Flux profiles

The flux profile in each province X is computed as the average flux across the province as below

$$F_{\text{provinceX}}(z) = \left(\frac{1}{\text{Area}_{\text{provinceX}}(z)}\right) \int_{(x,y)} \overline{F}(x,y,z)dxdy, \tag{3.8}$$

where $\text{Area}_{\text{provinceX}}(z)$ is the area of the province at each depth z. These fluxes are then used to compute TE at each province using the equation above. This is shown in Fig. 1(c) in the main manuscript.

3.4 Assumptions

In all the above, we only use output where the model is at least 1,080m deep. This excludes shallow areas such as shelves and coastal locations, but including them would introduce a significant bias to the export fluxes relative to the deep ocean transfer flux.

4 Reproducing Henson et al. (2012)

The Henson et al. (2012) [13] data compilation included global flux data at 41 locations spanning several regions of the world. These locations, however, are mostly concentrated in the Southern Ocean (below 45°S), Tropical areas (15°N-15°S), and both Northern Atlantic and Pacific oceans. These fluxes differ in date and sampling time length, and also in the methodology. The export fluxes (100m ± 20m) are thorium-derived, and in high latitudes were collected mostly in summer months while those in the tropics where collected all through the year. The deep ocean fluxes (2,000m) are annual mean based on deep-ocean sediment trap data, collected at different depths and extrapolated to 2,000m via the Martin curve with $b = 0.86$. The transfer efficiency is then calculated using these annually-averaged deep ocean fluxes divided by the short-sampled, localised export fluxes, with the results being extrapolated to the rest of the ocean via a relation with satellite data.

To compute TE according to their methodology, we randomly sampled 150 points (50 at each region below) from the aforementioned areas as follows:

- **Southern latitudes** (below 45°S): average over summer months (January-March) and computed TE at 50 randomly sampled locations;
- **Northern latitudes** (above 45°N): average over summer months (July-August) and computed TE at 50 randomly sampled locations;
- **Tropical latitudes** (15°N-15°S): average over the entire year and computed TE at 50 randomly sampled locations.

The same procedure was followed to compute the 1-year average upper-mesopelagic temperature (120m-540m) at each sampled location. An example of this sampling is shown in Fig. S.9.

We then performed both linear and nonlinear (exponential) regressions of this sampled TE and upper-mesopelagic temperature data, as shown in Fig. S.10. These are based on the following equations for TE as a function of $\text{Temp}_{\text{up-meso}}$:

$$\text{TE} = \alpha_{\text{linear}} \cdot \text{Temp}_{\text{up-meso}} + \beta_{\text{linear}}.$$

and

$$\text{TE} = \alpha_{\text{exp}} \cdot \left(e^{\beta_{\text{exp}} \cdot \left(\text{Temp}_{\text{up-meso}} - \text{Temp}_{\text{ref}}\right)}\right) + \text{TE}_{\text{ref}},$$

where $\alpha_{\text{linear}}, \beta_{\text{linear}}$ and $\alpha_{\exp}, \beta_{\exp}$ are the parameters to be fitted in the linear and nonlinear regressions. There, we chose $\text{Temp}_{\text{ref}} = 14$ and $\text{TE}_{\text{ref}} = 0.042$, which are based on the range of observed TE and and upper-mesopelagic temperature observed in the sampled model data.

To quantify the uncertainty, we repeated this procedure 10,000 times, with results shown in Tables S.1, S.2 and Figs. S.11, S.12. This resulted in the following regression relationships:

$$\text{TE} = 0.0028 \cdot \text{Temp}_{\text{up-meso}} + 0.0406. \tag{4.1}$$

$$\text{TE} = 0.0378 \cdot \left(e^{0.1620 \cdot \left(\text{Temp}_{\text{up-meso}} - 14\right)}\right) + 0.042. \tag{4.2}$$

We then used these relationships to infer the TE profiles, as shown in Figs. S.13 and S.14 for the linear and exponential parameterisations respectively. These are consistent with Henson et al. (2012) [13], showing TE that is higher at low latitudes and low at high latitudes.

References

[1] I. Kriest, S. Khatiwala, and A. Oschlies. Towards an assessment of simple global marine biogeochemical models of different complexity. *Progress in Oceanography*, 86(3):337 – 360, 2010.

[2] I. Kriest, A. Oschlies, and S. Khatiwala. Sensitivity analysis of simple global marine biogeochemical models. *Global Biogeochemical Cycles*, 26(2), 2012.

[3] Francisco de Melo Viríssimo, Adrian P. Martin, and Stephanie A. Henson. Influence of seasonal variability in flux attenuation on global organic carbon fluxes and nutrient distributions. *Global Biogeochemical Cycles*, 36(2):e2021GB007101, 2022.

[4] E. Kwon, F. Primeau, and J. Sarmiento. The impact of remineralization depth on the air–sea carbon balance. *Nature Geosciences*, 2:630–635, 2009.

[5] Roséanne Bol, Stephanie A. Henson, Anna Rumyantseva, and Nathan Briggs. High-frequency variability of small-particle carbon export flux in the northeast atlantic. *Global Biogeochemical Cycles*, 32(12):1803–1814, 2018.

[6] Stephanie. S. Kienast and Adi Torfstein. Evaluation of biological carbon pump metrics in the subtropical gulf of aqaba, northern red sea. *Global Biogeochemical Cycles*, 36(10):e2022GB007452, 2022. e2022GB007452 2022GB007452.

[7] Samar Khatiwala, Martin Visbeck, and Mark A. Cane. Accelerated simulation of passive tracers in ocean circulation models. *Ocean Modelling*, 9(1):51 – 69, 2005.

[8] Samar Khatiwala. A computational framework for simulation of biogeochemical tracers in the ocean. *Global Biogeochemical Cycles*, 21(3), 2007.

[9] Samar Khatiwala. samarkhatiwala/tmm: Version 2.0 of the transport matrix method software (2018, may 13). *Zenodo*, 2018.

[10] Thomas Weber, Jacob A. Cram, Shirley W. Leung, Timothy DeVries, and Curtis Deutsch. Deep ocean nutrients imply large latitudinal variation in particle transfer efficiency. *Proceedings of the National Academy of Sciences*, 113(31):8606–8611, 2016.

[11] Francisco de Melo Viríssimo, Adrian P. Martin, Stephanie A. Henson, and Jamie D. Wilson. Model output used in the manuscript "Seasonal variability in particle flux attenuation in the global ocean generates spatial variability in annual transfer efficiency" (v1.0). *Zenodo*, 2023.

[12] Jorge L. Sarmiento and Nicolas Gruber. *Ocean Biogeochemical Dynamics*. Princeton University Press, 2006.

[13] Stephanie A. Henson, Richard Sanders, and Esben Madsen. Global patterns in efficiency of particulate organic carbon export and transfer to the deep ocean. *Global Biogeochemical Cycles*, 26(1), 2012.

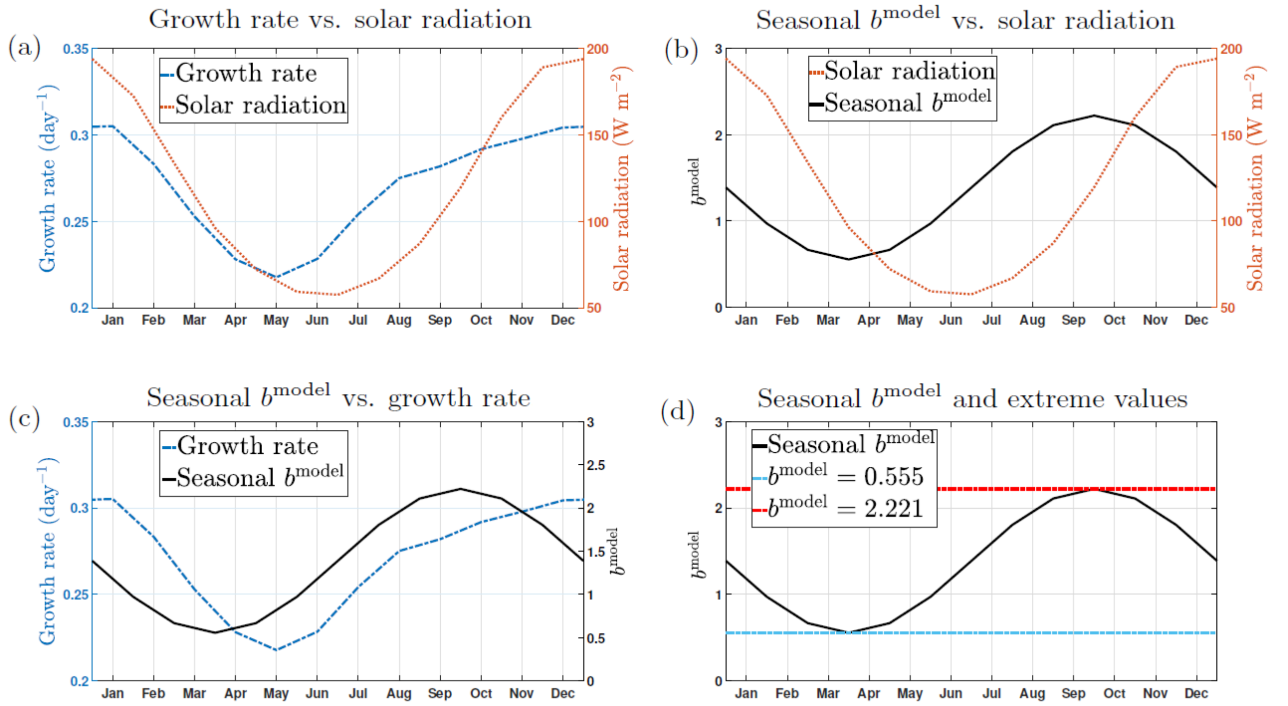

Figure S.1: Seasonal b^{model} in the Southern Hemisphere. Top: (a) Growth rate vs. solar radiation; (b) Seasonal b^{model} vs. solar radiation. Bottom: (c) Seasonal b^{model} vs. growth rate; (d) Seasonal b^{model} and extreme values. Versions of (a) and (b) also appear in de Melo Viríssimo et al. (2022) [3]

Table S.1: Statistics for linear regression in Equation (4.1) from a 10,000 random sample, p-value < 0.005.

linear regression parameters	R^2	α_{linear}	β_{linear}
μ (mean)	0.7326	0.0028	0.0406
σ (variance)	0.0286	1.0957e-04	6.4315e-04

Table S.2: Statistics for nonlinear (exponential) regression in Equation (4.2) from a 10,000 random sample, p-value < 0.005.

nonlinear (exponential) regression parameters	R^2	α_{exp}	β_{exp}
μ (mean)	0.7807	0.0378	0.1620
σ (variance)	0.0294	0.0015	0.0067

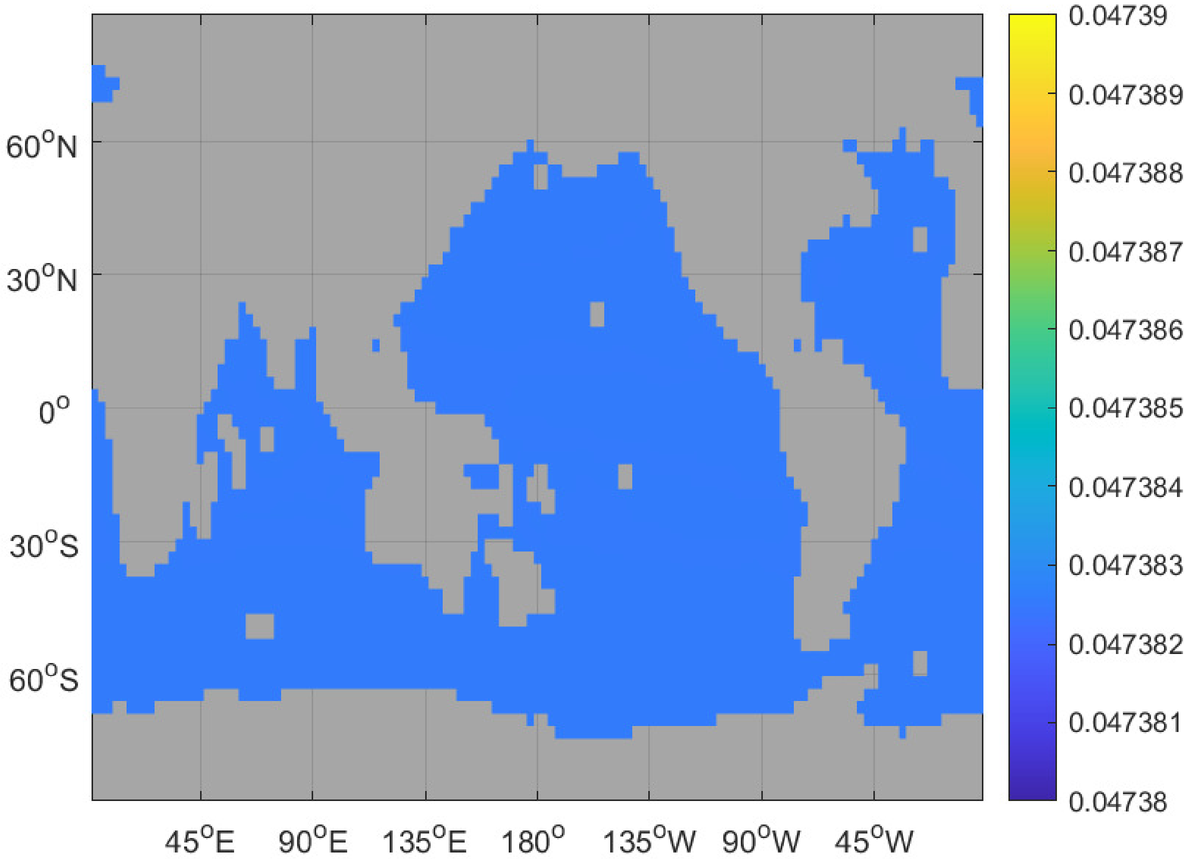

Figure S.2: Annual mean TE for a non-seasonal, constant $b^{\text{model}} = 1.388$. A version of this figure also appear in de Melo Viríssimo et al. (2022) [3]

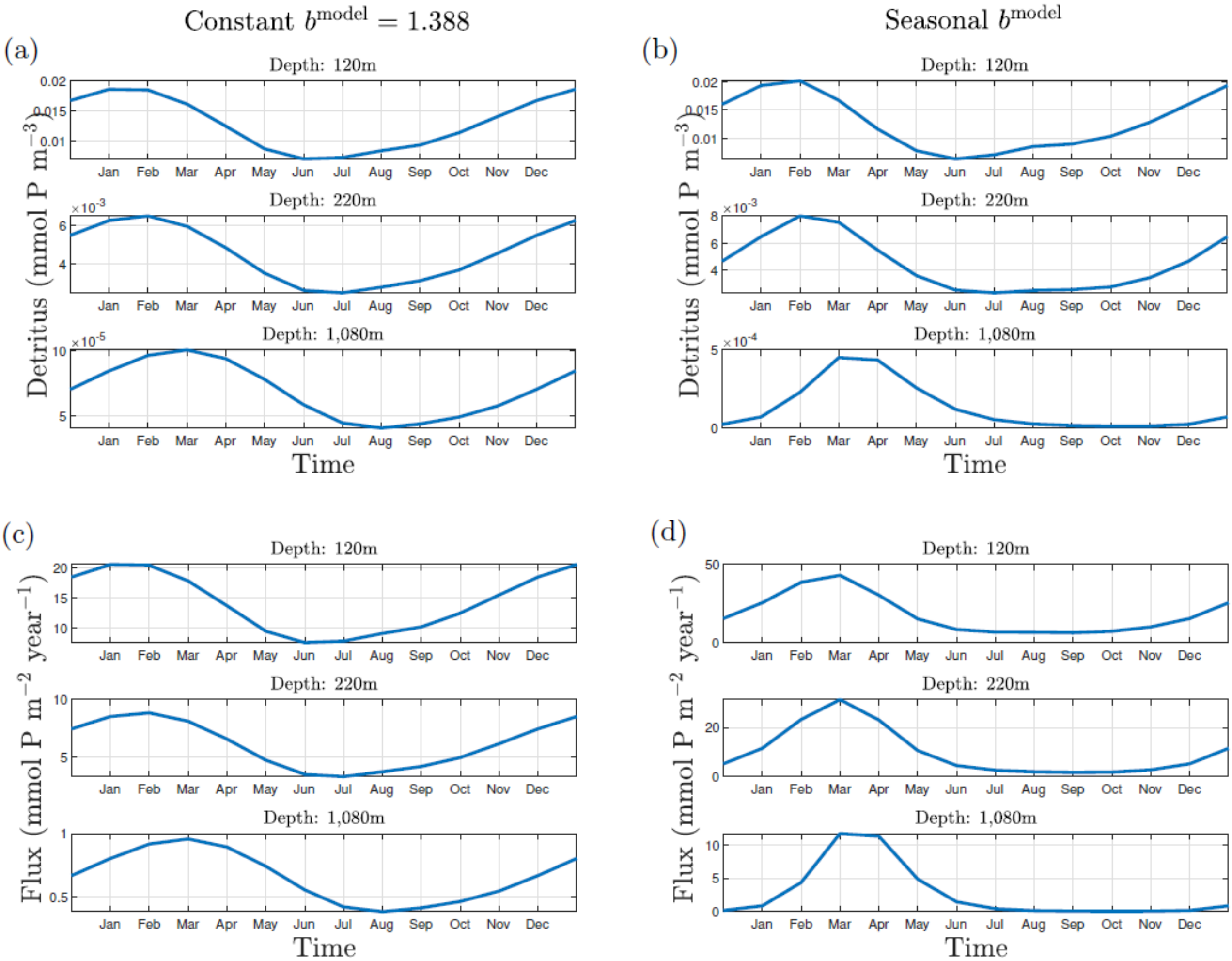

Figure S.3: Exported detritus attenuation in a constant and seasonal attenuation scenarios, when detritus is not transported by the ocean circulation. Top: time series for detritus concentration in the South Atlantic (43.59°S, 29.53°W) at different depths TE for (a) a constant $b^{\mathrm{model}} = 1.388$ and (b) a seasonal b^{model}. Bottom: time series for detritus flux for (c) $b^{\mathrm{model}} = 1.388$ and (d) a seasonal b^{model}.

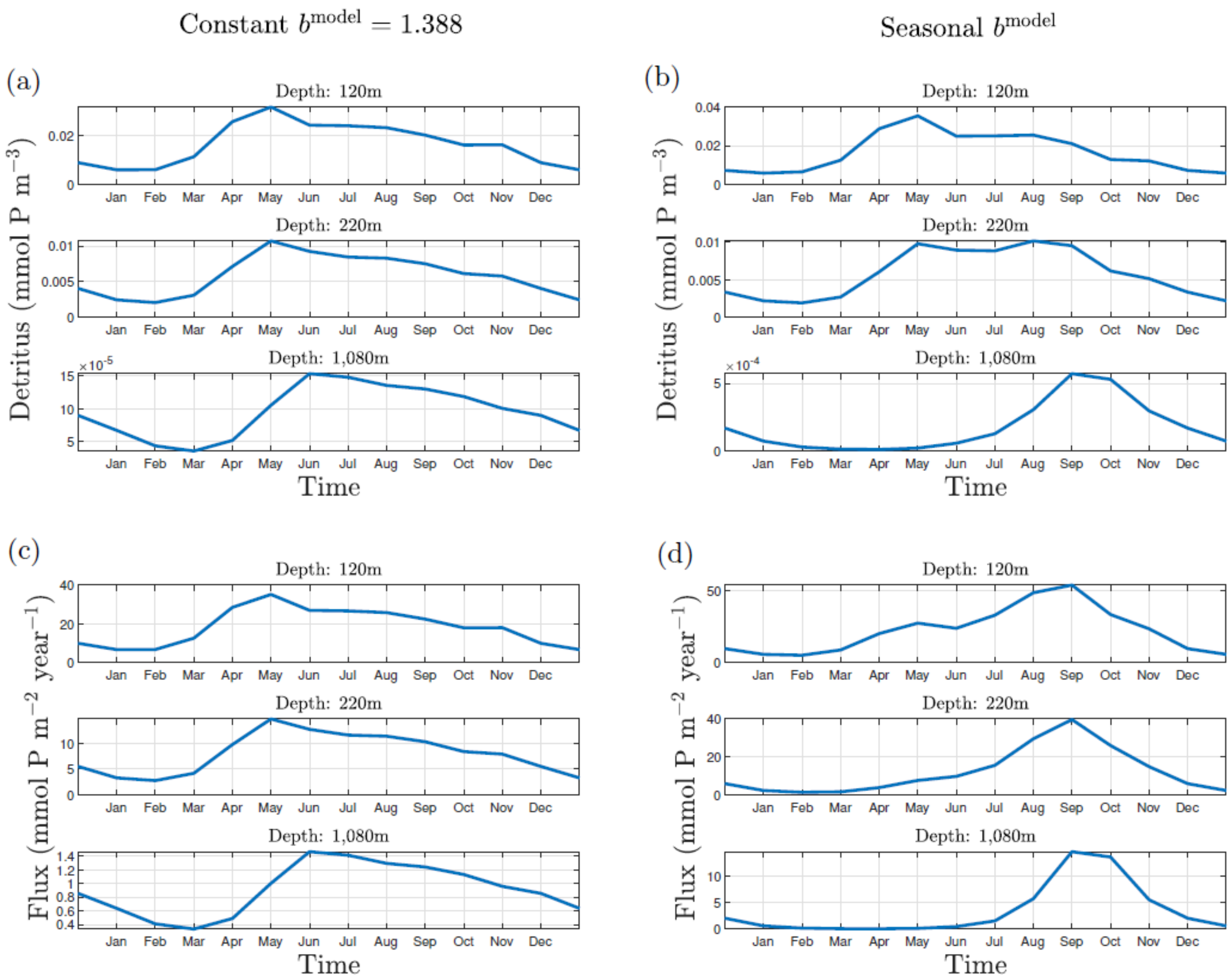

Figure S.4: Exported detritus attenuation in constant and seasonal attenuation scenarios, when detritus is not transported by the ocean circulation. Top: time series for detritus concentration in the North Atlantic (43.59°N, 35.52°W) at different depths for (a) a constant $b^{\mathrm{model}} = 1.388$ and (b) a seasonal b^{model}. Bottom: time series for detritus flux for (c) $b^{\mathrm{model}} = 1.388$ and (d) a seasonal b^{model}.

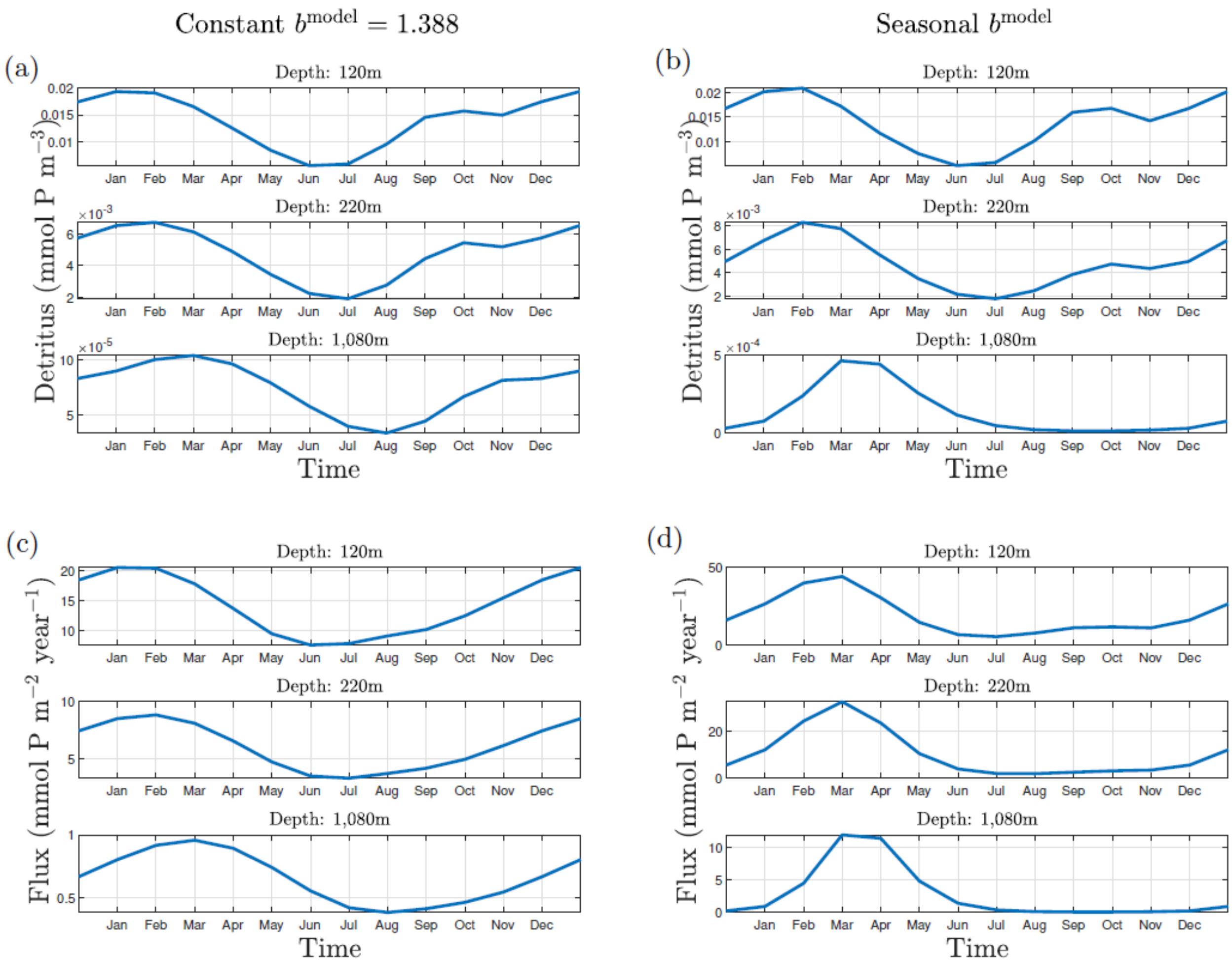

Figure S.5: Exported detritus attenuation in a constant and seasonal attenuation scenarios, when detritus is not transported by the ocean circulation. Top: time series for detritus concentration in the South Pacific (46.41°S, 150.47°W) at different depths TE for (a) a constant $b^{\mathrm{model}} = 1.388$ and (b) a seasonal b^{model}. Bottom: time series for detritus flux for (c) $b^{\mathrm{model}} = 1.388$ and (d) a seasonal b^{model}.

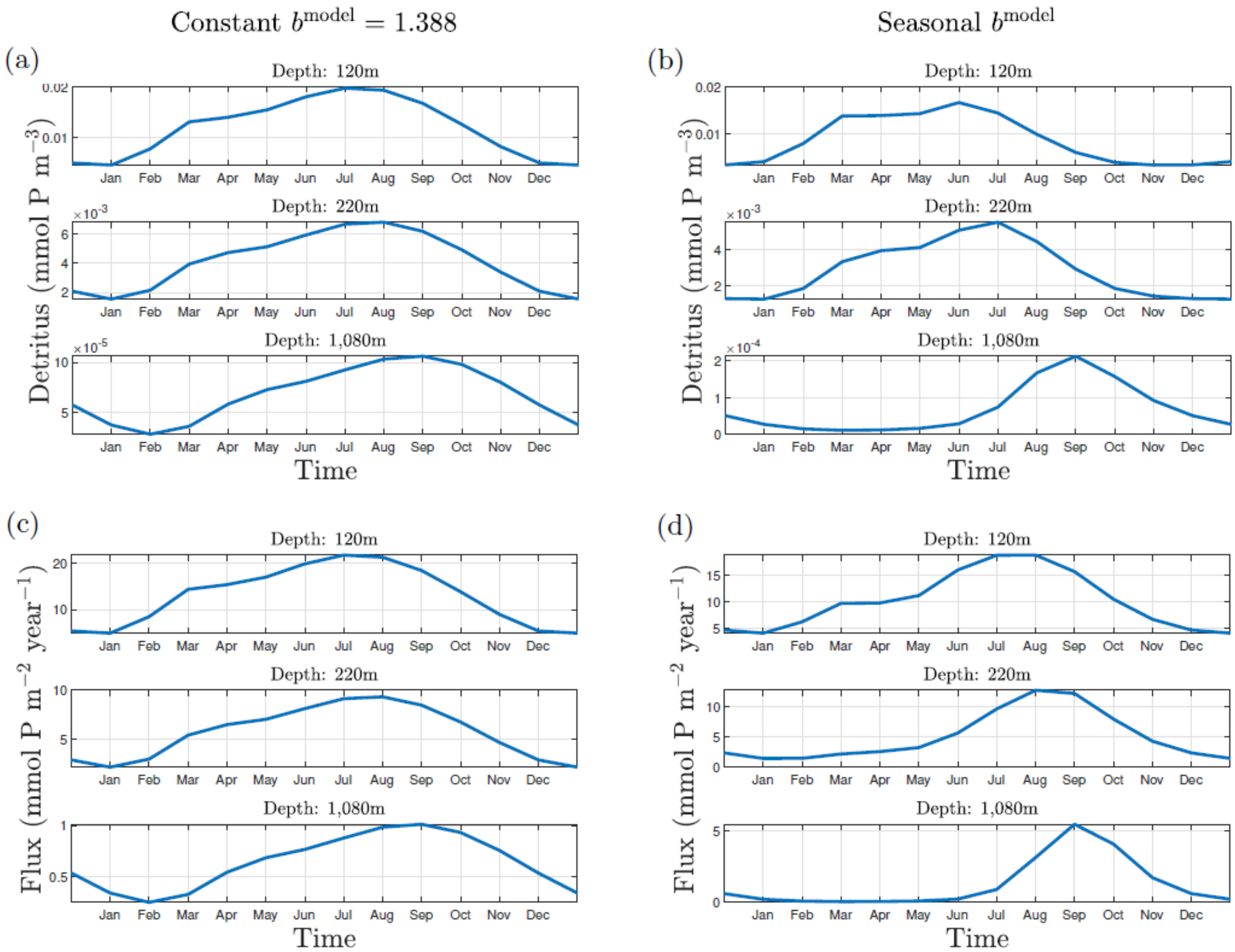

Figure S.6: Exported detritus attenuation in a constant and seasonal attenuation scenarios, when detritus is not transported by the ocean circulation. Top: time series for detritus concentration in the North Pacific (49.21°N, 136.41°W) at different depths TE for (a) a constant $b^{\mathrm{model}} = 1.388$ and (b) a seasonal b^{model}. Bottom: time series for detritus flux for (c) $b^{\mathrm{model}} = 1.388$ and (d) a seasonal b^{model}.

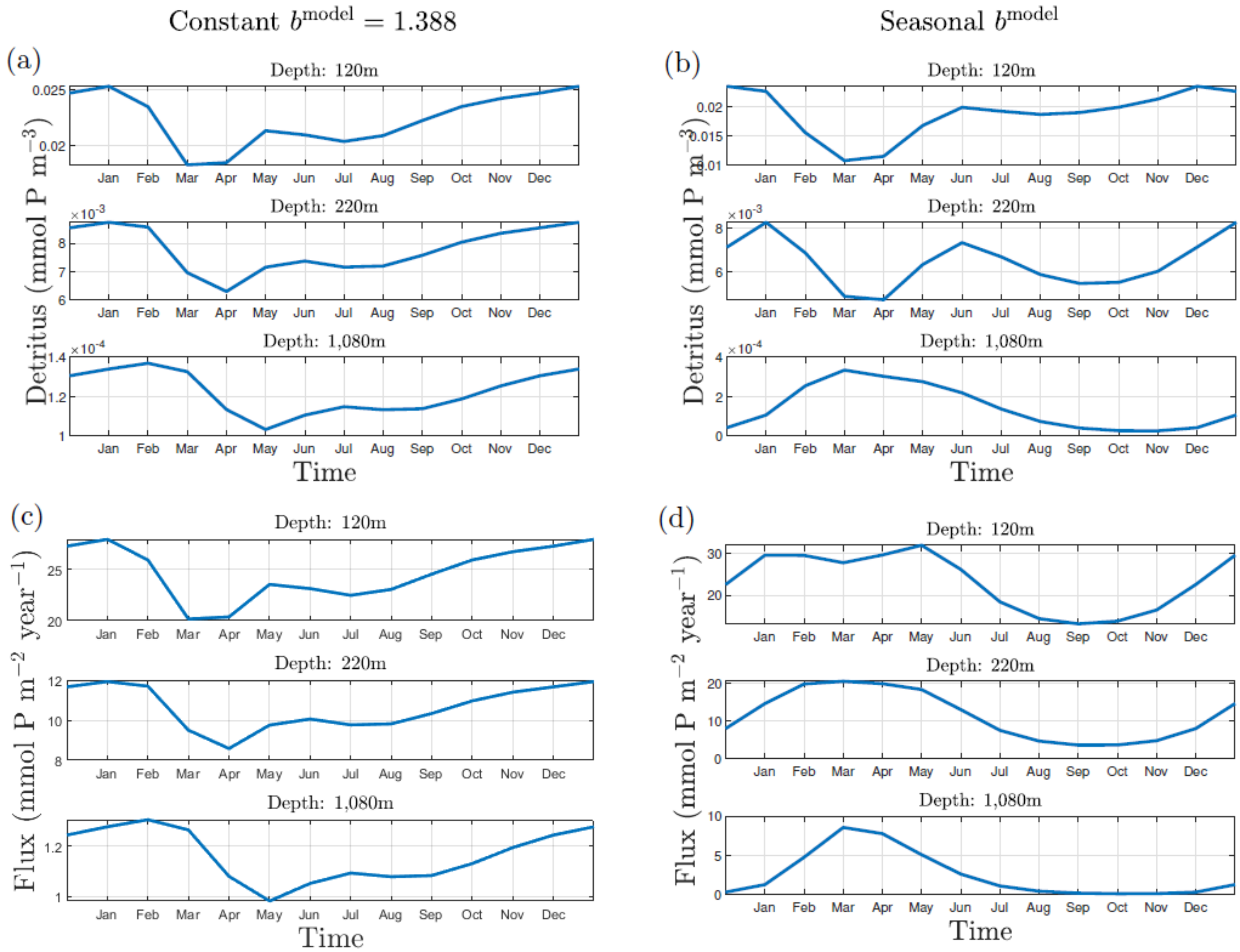

Figure S.7: Exported detritus attenuation in a constant and seasonal attenuation scenarios, when detritus is not transported by the ocean circulation. Top: time series for detritus concentration in the Indian (7.03°S, 74.53°E) at different depths TE for (a) a constant $b^{\text{model}} = 1.388$ and (b) a seasonal b^{model}. Bottom: time series for detritus flux for (c) $b^{\text{model}} = 1.388$ and (d) a seasonal b^{model}.

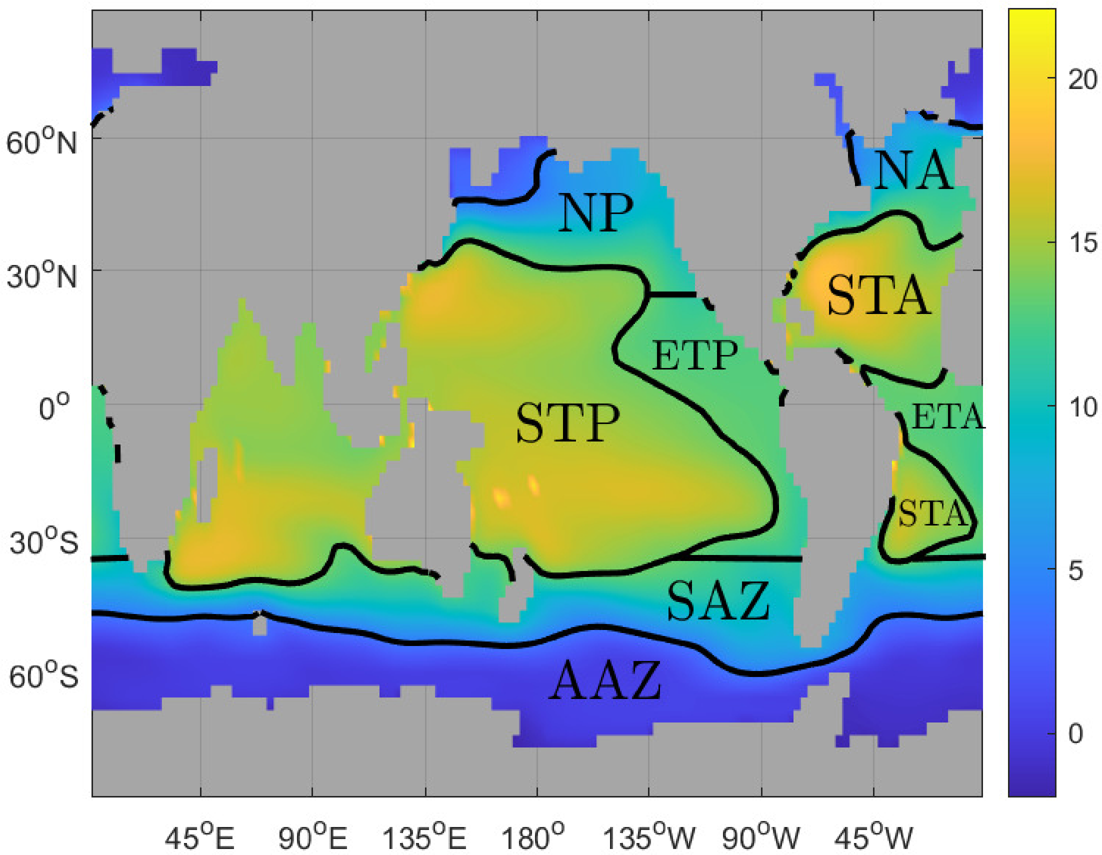

Figure S.8: Annual mean upper-mesopelagic temperature (in °C) with ocean provinces.

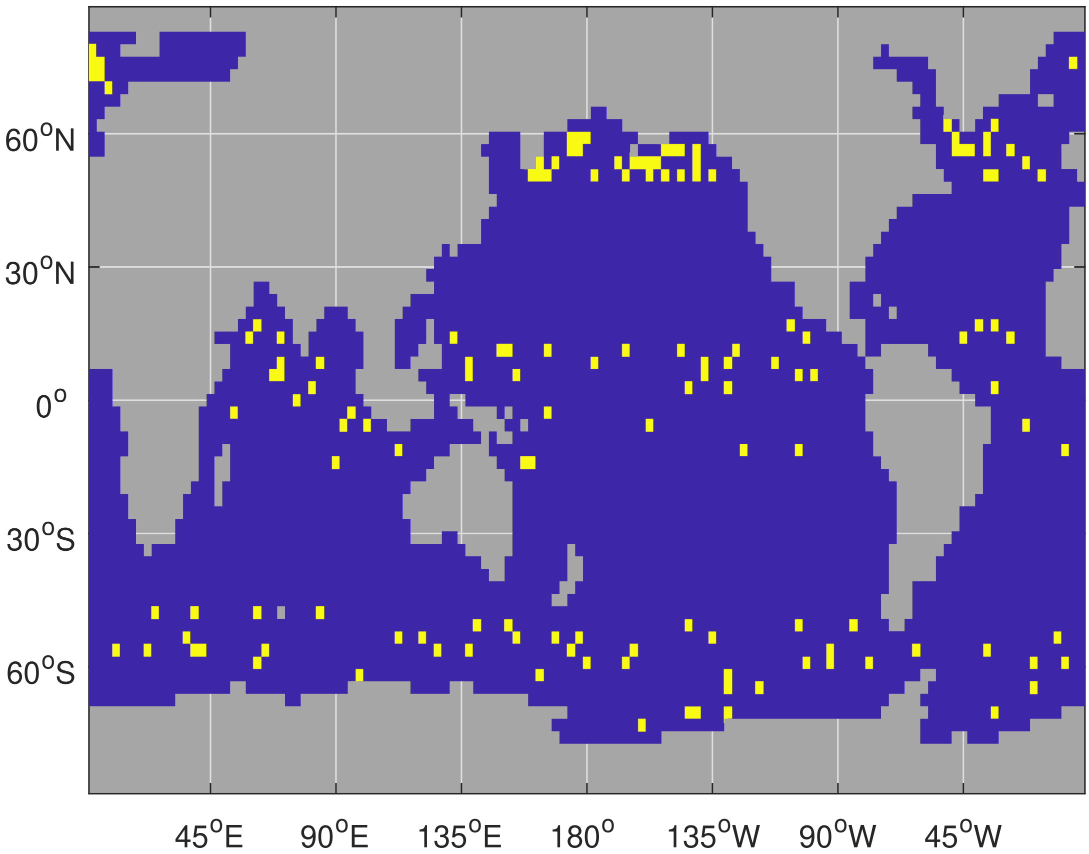

Figure S.9: Example of randomly sampled locations from model data.

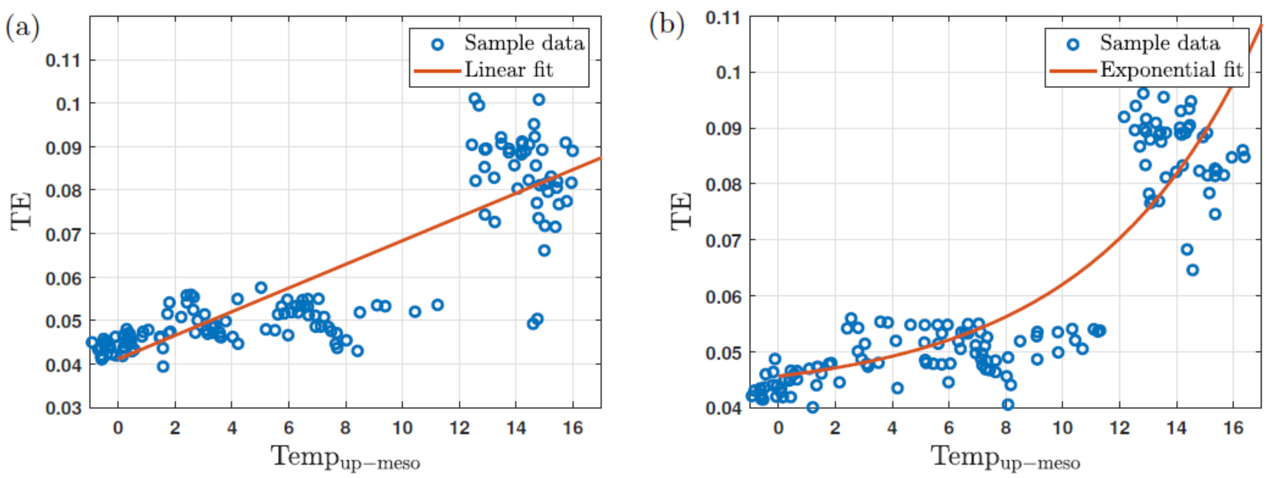

Figure S.10: Examples of statistical regression done using a random sample from model data: (a) linear fit; (b) exponential fit.

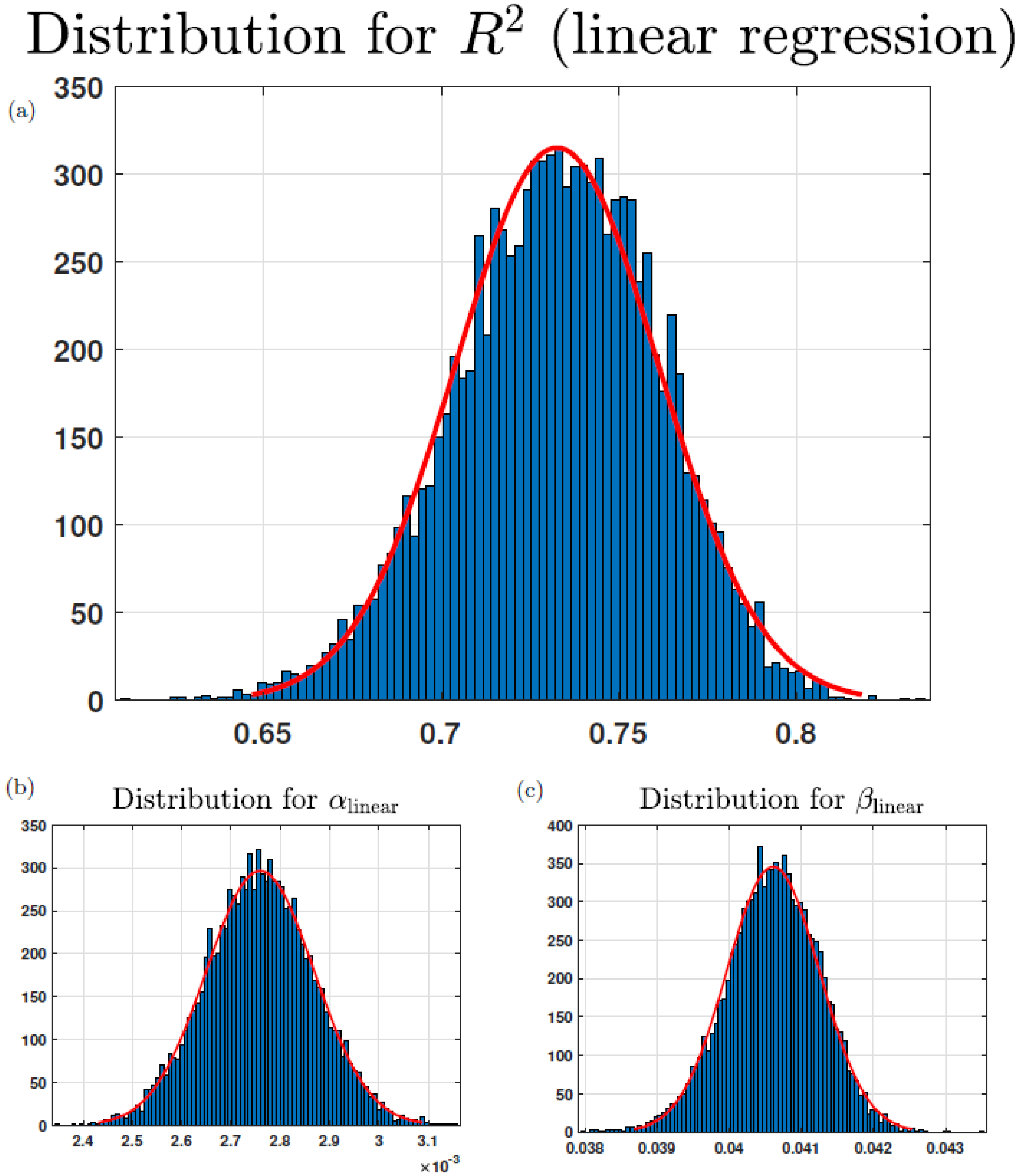

Figure S.11: Results from a TE versus temperature linear regression for 10,000 randomised samples. Top: (a) R^2 for a 10,000 random sample. Bottom: (b) Distribution for α_{linear}; (c) Distribution for β_{linear}.

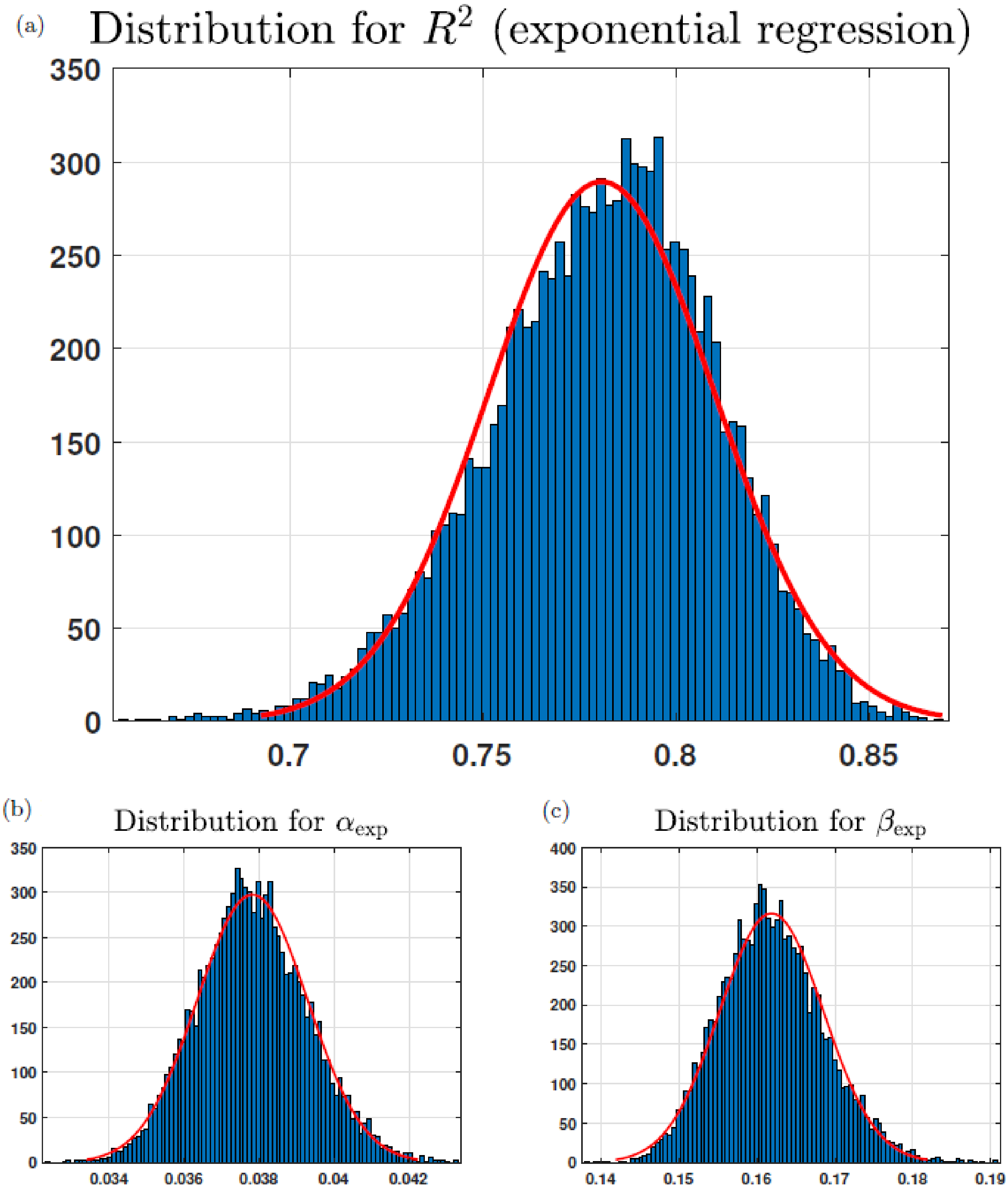

Figure S.12: Results from a TE versus temperature nonlinear (exponential) regression for 10,000 randomised samples. Top: (a) R^2 for a 10,000 random sample. Bottom: (b) Distribution for α_{exp}; (c) Distribution for β_{exp}.

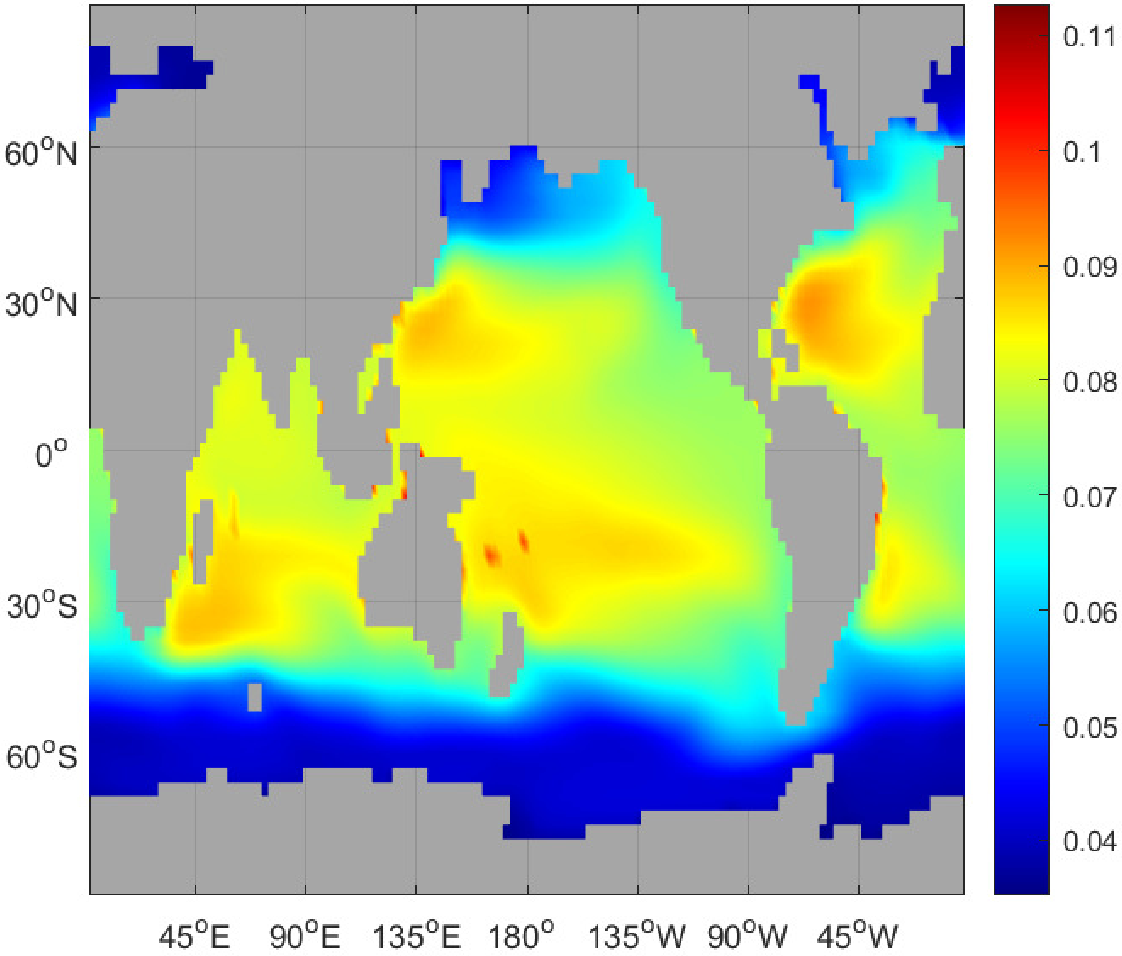

Figure S.13: Annual mean TE obtained from a linear regression in Equation (4.1), which follows the procedure of Henson et al. (2012).

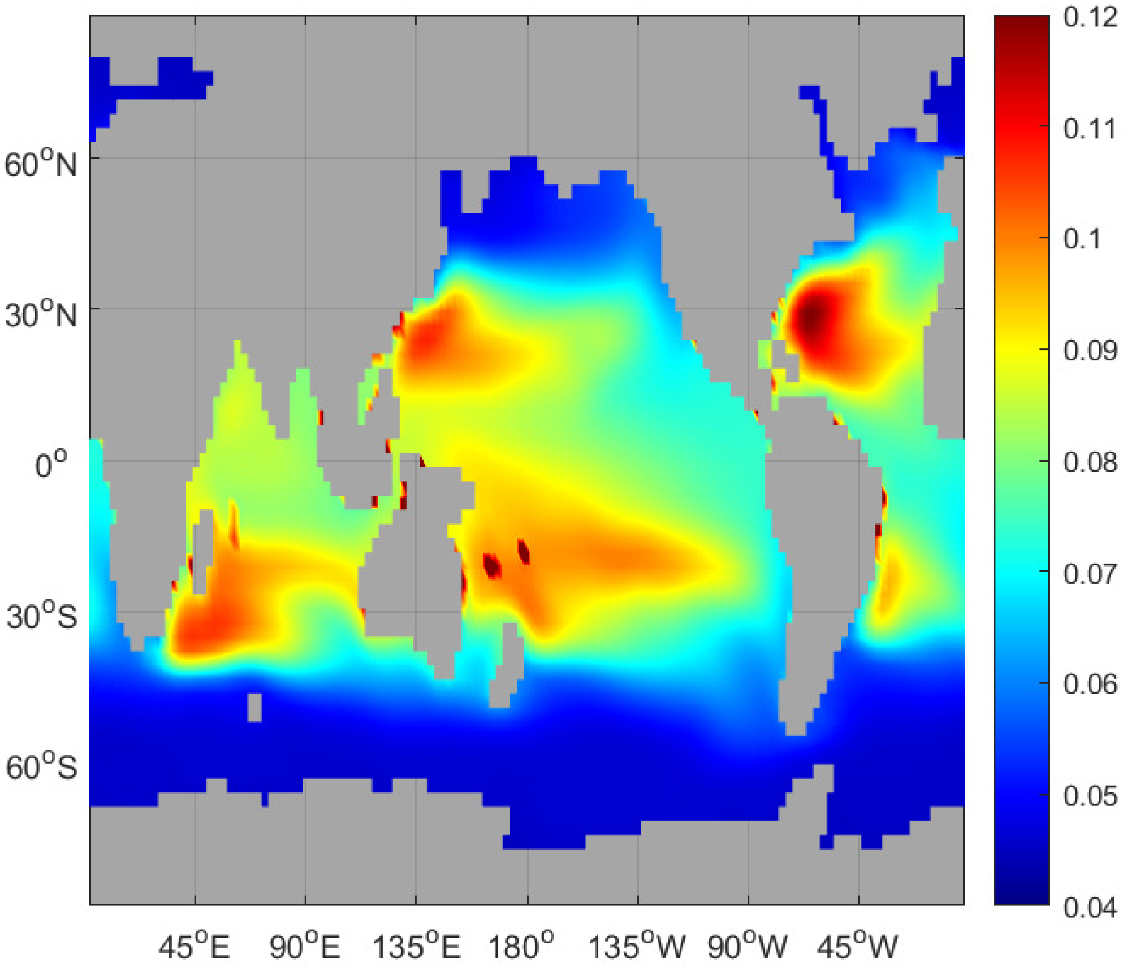

Figure S.14: Annual mean TE obtained from a nonlinear (exponential) regression in Equation (4.2), which follows the procedure of Henson et al. (2012).